INTERNATIONAL JOURNAL FOR NUMERICAL METHODS IN FLUIDS, VOL. 24, 17–59 (1997)

A MULTI-LEVEL NUMERICAL MODEL OF COASTAL UPWELLING: A DIAGNOSTIC STUDY

A. D. RAO AND S. CHAMARTHI

Centre for Atmospheric Sciences, Indian Institute of Technology Delhi, Hauz Khas, New Delhi–110 016, India

SUMMARY

A two-dimensional baroclinic model is described for coastal upwelling in a vertical plane perpendicular to the coast. The model consists of equations of motion, continuity and turbulence energy along with equations for salinity and thermal energy and an equation of state. The role of density gradient in the baroclinic pressure gradient is investigated to understand the dynamics during the upwelling process. To represent the surface and bottom boundaries corresponding to a fixed computational level in the discretized equations, a set of non-dimensional co-ordinates is used. These co-ordinates are then transformed onto logarithmic co-ordinate axes to resolve effectively the boundary layers.

The first experiment is carried out with a flat bottom to understand the dynamics of the upwelling and the structural features of the process by diagnostic analysis of the balance between various terms of the momentum equation. Starting from a state of rest, a spatially uniform alongshore wind stress corresponding to the mean monthly wind stress for the month of May is applied and held constant thereafter. The fluid is assumed to be incompressible and stratified, with the initial temperature and salinity having no horizontal variations but a uniform vertical gradient. As the upwelling phenomenon is transient in nature and keeping in mind the additional computational overheads, the response of the model is studied day-wise up to 4 days.

In the second experiment the model is applied to study the upwelling off the east coast of India in a plane normal to the coast of Visakhapatnam. The analysis area extends to 100 km offshore with real topography. The results are presented day-wise for 4 days, comparing the balance between various terms in the upwelling region and in the open sea, and the dynamics of the baroclinic coastal jet is explained.

KEY WORDS: radiation boundary condition; numerical model; coastal upwelling; baroclinic model; coastal jet

1. INTRODUCTION

Regions of coastal upwelling are characterized by a reduction in the sea surface temperature and high biological activity. First available observations of the coastal upwelling along the east coast of India from Lafong[1] indicate that upwelling of subsurface layers of the sea occurs from March to May and sinking of surface layers takes place from September to November along the central part of the coast. Observations of Rao *et al.*[2] reveal that upwelling is predominant off Visakhapatnam during pre-monsoon periods and then decreases with the withdrawal of the south-west monsoon.

Early models of coastal upwelling mostly assumed the water to be homogeneous, leading to little practical application except for providing an indication of water movements. These models, with very few exceptions,[3] are linearized. However, the non-linearities cannot generally be rejected; for example, the horizontal temperature and salinity variation, which result in offshore advection of

CCC 0271–2091/97/010017–43

Received August 1995
Revised February 1996

upwelled cold water in the surface layer, has a significant effect on the dynamics of the upwelling. Also, the linear models are constrained by many assumptions to obtain the solutions, e.g. use of simple parametrization of turbulent mixing processes (constant coefficients of eddy viscosity and diffusivity[4]) unrealistic boundary conditions (fixed temperature at the surface[4,5]) etc. Thus the study of the dynamics of upwelling needs a numerical model to solve the interactions involved in the complicated non-linear problems.

O'Brien and Hulbert[6] formulated a two-dimensional layered model for studying the dynamics of the upwelling on an f-plane. The model is time-dependent and with no alongshore gradients. To simplify matters, they have not considered the exchange of heat, momentum and mass between the layers, which is an essential part of coastal dynamics.

Herein a two-dimensional non-linear model is described with a continuously stratified ocean to account for the exchange of heat, momentum and mass. The model is based upon the dynamical framework described by Johns *et al.*,[7] consisting of the continuity equation, the equations of motion and a turbulent energy equation to parameterize the vertical transfer of momentum and turbulence energy. In the present study the effect of the baroclinic pressure gradient term resulting from a horizontal density gradient is included in the horizontal momentum equation along with an equation of state connecting the temperature and salinity. Also, the effect of a stable vertical density stratification on the production of turbulence is taken into account by the inclusion of a vertical density gradient term in the turbulence energy equation.

To facilitate the resolution of boundary layers, a set of non-dimensional co-ordinates analogous to that used by Phillips[8] and Freeman *et al.*[9] is adopted such that the boundaries correspond to fixed computational levels in the discretization of the equations. These non-dimensional co-ordinates are then further transformed onto stretched logarithmic axes. Thus the desired resolution in the boundary layer has been attained without introducing an excess number of computational levels.

2. FORMULATION

2.1. Governing equations

Right-handed rectangular axes are chosen, assuming that the curvature of the earth's surface can be neglected. The origin O is situated at the coastline and at the mean sea level. The axes Ox, Oy and Oz point offshore, alongshore and vertically upwards respectively. The elevation of the sea surface above its mean sea level $z = 0$ is denoted by $z = \zeta(x, t)$ and the bottom topography by $z = -h(x)$. The coastal boundary corresponds to $x = 0$ and the eastern open-sea boundary to $x = L_x$. Figure 1 shows schematically the model geometry and rectangular axes.

The dynamical equations consist of the equations of motion, the equations for mass conservation, thermal energy and salinity and the equation of state. These equations are supplemented by the turbulence energy density equation together with Kolmogorov's hypothesis.

The equations of motion in the directions x, y and z respectively are of the form

$$\frac{\partial u}{\partial t} + u\frac{\partial u}{\partial x} + w\frac{\partial u}{\partial z} - fv = -\frac{1}{\rho_0}\frac{\partial p}{\partial x} + \frac{1}{\rho_0}\frac{\partial \tau_x}{\partial z}, \tag{1}$$

$$\frac{\partial v}{\partial t} + u\frac{\partial v}{\partial x} + w\frac{\partial v}{\partial z} + fu = \frac{1}{\rho_0}\frac{\partial \tau_y}{\partial z}, \tag{2}$$

$$0 = -\frac{1}{\rho}\frac{\partial p}{\partial z} - g, \tag{3}$$

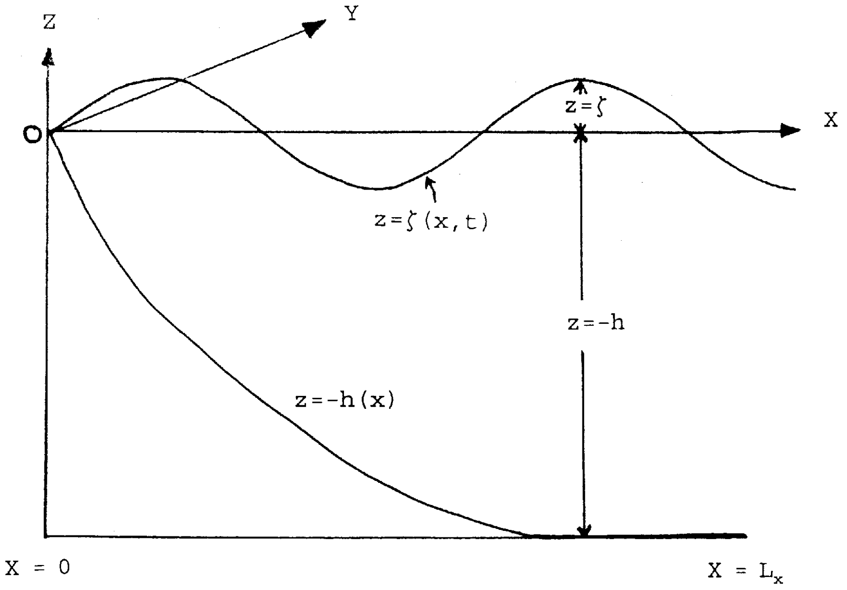

Figure 1. Model geometry and rectangular axes

where u, v and w are the velocity components parallel to the axes x, y and z respectively, τ_x and τ_y are the components of turbulent shear stress in the directions x and y respectively, p is the pressure, f is the Coriolis parameter, ρ_0 is the reference density of the water, ρ is the density of the water, g is the acceleration due to gravity and t is the time.

The shear components τ_x and τ_y are related to the velocity components u and v, using the gradient transfer hypothesis, by

$$\tau_x = \rho_0 K_\mathrm{M} \frac{\partial u}{\partial z}, \qquad \tau_y = \rho_0 K_\mathrm{M} \frac{\partial v}{\partial z}, \tag{4a, b}$$

where K_M is defined as the vertical exchange coefficient for momentum and is determined by Kolmogorov's hypothesis.

Assuming that the fluid is incompressible, the equation of continuity is expressed as

$$\frac{\partial u}{\partial x} + \frac{\partial w}{\partial z} = 0. \tag{5}$$

The temperature T and salinity S are determined from transport equations of the form

$$\frac{\partial T}{\partial t} + u\frac{\partial T}{\partial x} + w\frac{\partial T}{\partial z} = \frac{\partial}{\partial z}\left(K_\mathrm{T}\frac{\partial T}{\partial z}\right), \tag{6}$$

$$\frac{\partial S}{\partial t} + u\frac{\partial S}{\partial x} + w\frac{\partial S}{\partial z} = \frac{\partial}{\partial z}\left(K_\mathrm{S}\frac{\partial S}{\partial z}\right). \tag{7}$$

The equation of state, in which the temperature and salinity are related linearly to the density, is

$$\rho = \rho_0[1 - \alpha(T - T_0) + \delta(S - S_0)], \tag{8}$$

where α is the thermal expansion coefficient, taken as $2{\cdot}0 \times 10^{-4}\ {}^{\circ}\mathrm{C}^{-1}$, δ is the coefficient of expansion for salinity, taken as $7{\cdot}5 \times 10^{-4}\ \mathrm{ppt}^{-1}$, and T_0 and S_0 are the reference temperature and salinity respectively.

The turbulence energy density E is determined from the equation

$$\frac{\partial E}{\partial t} + u\frac{\partial E}{\partial x} + w\frac{\partial E}{\partial z} = K_{\mathrm{M}}\left[\left(\frac{\partial u}{\partial z}\right)^2 + \left(\frac{\partial v}{\partial z}\right)^2\right] + \frac{\partial}{\partial z}\left(K_{\mathrm{E}}\frac{\partial E}{\partial z}\right) + \frac{g}{\rho_0}K_{\mathrm{D}}\frac{\partial \rho}{\partial z} - \varepsilon, \tag{9}$$

where K_{E} and K_{D} are the exchange coefficients for turbulence energy density and density respectively. The first term on the right-hand side of (9) represents the effect of the turbulence production by energy extraction due to the vertical shear in the mean flow. The second term represents the vertical diffusion of E. The third term gives the positive or negative contribution to the production of E depending upon the vertical density stratification. The last term simulates dissipation ε and is parameterized as

$$\varepsilon = c^{3/4}E^{3/2}/l, \tag{10}$$

where c is a constant with the value 0·08 and l is a turbulent mixing length scale chosen to be consistent with a reduction in vertical mixing near the boundaries $z = -h$ and ζ. Accordingly, a modified Prandtl mixing length scale is used as

$$l = \frac{\kappa}{1/\lambda_1 + 1/\lambda_2}, \tag{11}$$

where

$$\lambda_1 = (z + h + z_{0\mathrm{b}}), \qquad \lambda_2 = (\zeta - z + z_{0\mathrm{s}}). \tag{12a, b}$$

In (11), κ is Von Karman's constant and $z_{0\mathrm{s}}$ and $z_{0\mathrm{b}}$ are parameters related to the roughness of the sea surface and sea floor respectively. Thus the mixing length scale l reaches a maximum value in the mid-depth region and decreases towards both the sea surface and the sea floor. Also, (11) reduces to Prandtl's length scale given by (12a) and (12b) in the regions adjacent to the sea floor and sea surface, which results in the well-documented logarithmic velocity profile within these regions provided that sufficient resolution is available in the numerical solution.

Following Li,[10] the exchange coefficients are given by

$$K_{\mathrm{M}} = c^{1/4}lE^{1/2} + N, \tag{13}$$

$$K_{\mathrm{D}} = K_{\mathrm{S}} = K_{\mathrm{T}} = K_{\mathrm{E}} = c^{1/4}lE^{1/2}. \tag{14}$$

In (13), N is an externally prescribed mixing coefficient which reduces to negligible values near both the sea surface and the sea floor. The characteristic mid-depth value of N is $10^{-2}\ \mathrm{m}^2\ \mathrm{s}^{-1}$. This type of vertical distribution is chosen to increase the vertical turbulent exchange of momentum in the mid-depths compared with salinity, thermal and turbulent energy. Utilizing the fact that the vertical grid spacing Δz is relatively coarser in the mid-depths compared with its values near the sea floor and sea surface, the prescribed form used for N is made proportional to the local value of Δz. Giving the physical justification for the implementation of the procedure, Kundu[11] has described how the vertical transfer of momentum is supported by small-scale turbulence and large-scale internal gravity waves. Transfer by the latter is dominant in regions of strong stable thermal stratification where the shear production of small-scale turbulence is suppressed.[12] Since the internal gravity waves are not solved in this model, their effect is parametrized by the vertical mixing enhancement procedure in regions where the turbulence energy E diminishes to negligible values. An alternative approach may be to use the concept of stability functions.[13]

2.2. Boundary conditions

At the sea surface $z = \zeta(x, t)$ the boundary conditions to be satisfied are

$$\frac{\partial \zeta}{\partial t} + u\frac{\partial \zeta}{\partial x} - w = 0, \tag{15a}$$

$$K_\mathrm{M}\frac{\partial u}{\partial z} = \frac{\tau_x^\zeta}{\rho_0}, \qquad K_\mathrm{M}\frac{\partial v}{\partial z} = \frac{\tau_y^\zeta}{\rho_0}, \tag{15b, c}$$

$$\frac{\partial T}{\partial z} = \frac{\partial S}{\partial z} = \frac{\partial E}{\partial z} = 0, \tag{15d}$$

where τ_x^ζ and τ_y^ζ are the applied surface wind stresses in the directions x and y respectively.

At the sea floor $z = -h(x)$ the boundary conditions are

$$u = v = 0, \tag{16a}$$

$$\frac{\partial T}{\partial z} = \frac{\partial S}{\partial z} = \frac{\partial E}{\partial z} = 0, \tag{16b}$$

$$w = -u\frac{\partial h}{\partial x}. \tag{16c}$$

At the western boundary $x = 0$ the boundary condition is

$$u = 0. \tag{17}$$

At the eastern open-sea boundary $x = L_x$ a radiation condition is applied to determine the elevation of the sea surface,

$$\bar{u} - (g/h)^{1/2}\zeta = 0, \tag{18}$$

where $\bar{u}$ is the depth-averaged velocity in the x-direction, given by

$$\bar{u} = \frac{1}{H}\int_{-h}^{\zeta} u \,\mathrm{d}z.$$

The temperature and salinity at the open-sea boundary are determined according to the direction of the fluid flow. During outflow it is determined by the horizontal advection from the interior and during inflow it is determined by the advection invoking the temperature and salinity just outside the analysis region. The temperature and salinity just outside the analysis region are assumed to be known and are taken as temporally invariant during the integration. The exact way in which the boundary conditions are applied will be seen more clearly in Section 5.

The horizontal pressure gradient can be expressed in terms of a barotropic component arising from the variations in the sea surface elevation and a baroclinic component which expresses the buoyancy arising from the horizontal density gradient:

$$-\frac{1}{\rho_0}\frac{\partial p}{\partial x} = -g\frac{\partial \zeta}{\partial x} - \frac{g}{\rho_0}\int_{z}^{\zeta}\frac{\partial \rho}{\partial x}\,\mathrm{d}z. \tag{19}$$

Making use of (4), (8) and (19), equations (1), (2) and (9) can be written as

$$\frac{\partial u}{\partial t}+u\frac{\partial u}{\partial x}+w\frac{\partial u}{\partial z}-fv=-g\frac{\partial \zeta}{\partial x}+g\left(\alpha\int_z^{\zeta}\frac{\partial T}{\partial x}\,\mathrm{d}z-\delta\int_z^{\zeta}\frac{\partial S}{\partial x}\,\mathrm{d}z\right)+\frac{\partial}{\partial z}\left(K_{\mathrm{M}}\frac{\partial u}{\partial z}\right), \qquad (20)$$

$$\frac{\partial v}{\partial t}+u\frac{\partial v}{\partial x}+w\frac{\partial v}{\partial z}+fu=\frac{\partial}{\partial z}\left(K_{\mathrm{M}}\frac{\partial v}{\partial z}\right), \qquad (21)$$

$$\frac{\partial E}{\partial t}+u\frac{\partial E}{\partial x}+w\frac{\partial E}{\partial z}=K_{\mathrm{M}}\left[\left(\frac{\partial u}{\partial z}\right)^2+\left(\frac{\partial v}{\partial z}\right)^2\right]+\frac{\partial}{\partial z}\left(K_{\mathrm{E}}\frac{\partial E}{\partial z}\right)-g\left(\alpha K_{\mathrm{T}}\frac{\partial T}{\partial z}-\delta K_{\mathrm{s}}\frac{\partial S}{\partial z}\right)-\varepsilon. \qquad (22)$$

Using the kinematical free surface boundary condition, the continuity equation is expressed as

$$\frac{\partial \zeta}{\partial t}+\frac{\partial}{\partial x}(H\bar{u})=0. \qquad (23)$$

Hence (20)–(23) and (5)–(7) form the basic dynamical equations of the model.

3. CO-ORDINATE TRANSFORMATION

In the above rectangular Cartesian co-ordinates the sea surface and sea floor may not correspond to fixed computational levels in the discretization of the equations, which could lead to a rather crude representation of the boundary conditions. A transformation of the vertical co-ordinate into a non-dimensional vertical co-ordinate σ is therefore introduced as

$$\sigma=(z+h)/H, \qquad (24)$$

where $H=\zeta+h$ is the total depth of the water. Thus σ increases monotonically from $\sigma=0$ at the bottom $z=-h(x)$ to $\sigma=1$ at the free surface $z=\zeta(x,t)$, simplifying the application of the boundary conditions at the fixed computational levels $\sigma=0$ and 1.

Similar to the vertical co-ordinate transformation, a new non-dimensional horizontal co-ordinate χ can be used to replace x,

$$\chi=x/L_x, \qquad (25)$$

so that $\chi=0$ and 1 correspond to the western boundary ($x=0$) and eastern open-sea boundary ($x=L_x$) respectively.

Taking (χ,σ,t) as new independent co-ordinates, equations (20), (21), (5), (23), (6), (7) and (22) may be readily transformed into

$$\begin{aligned}\frac{\partial u}{\partial t}+\frac{u}{L_x}\frac{\partial u}{\partial \chi}+\omega\frac{\partial u}{\partial \sigma}-fv=&-\frac{g}{L_x}\frac{\partial \zeta}{\partial \chi}+g\alpha\left\{\int_\sigma^1\frac{1}{L_x}\frac{\partial}{\partial \chi}(HT)\,\mathrm{d}\sigma-\frac{1}{L_x}\left[\frac{\partial \zeta}{\partial \chi}T_{\sigma=1}+\left(\frac{\partial h}{\partial \chi}-\sigma\frac{\partial H}{\partial \chi}\right)T\right]\right\}\\&-g\delta\left\{\int_\sigma^1\frac{1}{L_x}\frac{\partial}{\partial \chi}(HS)\,\mathrm{d}\sigma-\frac{1}{L_x}\left[\frac{\partial \zeta}{\partial \chi}S_{\sigma=1}+\left(\frac{\partial h}{\partial \chi}-\sigma\frac{\partial H}{\partial \chi}\right)S\right]\right\}\\&+\frac{1}{H^2}\frac{\partial}{\partial \sigma}\left(K_{\mathrm{M}}\frac{\partial u}{\partial \sigma}\right),\end{aligned} \qquad (26)$$

$$\frac{\partial v}{\partial t}+\frac{u}{L_x}\frac{\partial v}{\partial \chi}+\omega\frac{\partial v}{\partial \sigma}+fu=\frac{1}{H^2}\frac{\partial}{\partial \sigma}\left(K_{\mathrm{M}}\frac{\partial v}{\partial \sigma}\right), \tag{27}$$

$$\frac{\partial \zeta}{\partial t}+\frac{1}{L_x}\frac{\partial}{\partial \chi}(Hu)+\frac{\partial \omega}{\partial \sigma}=0, \qquad \frac{\partial \zeta}{\partial t}+\frac{1}{L_x}\frac{\partial}{\partial \chi}(H\bar{u})=0, \tag{28a, b}$$

$$\frac{\partial T}{\partial t}+\frac{u}{L_x}\frac{\partial T}{\partial \chi}+\omega\frac{\partial T}{\partial \sigma}=\frac{1}{H^2}\frac{\partial}{\partial \sigma}\left(K_{\mathrm{T}}\frac{\partial T}{\partial \sigma}\right), \tag{29}$$

$$\frac{\partial S}{\partial t}+\frac{u}{L_x}\frac{\partial S}{\partial \chi}+\omega\frac{\partial S}{\partial \sigma}=\frac{1}{H^2}\frac{\partial}{\partial \sigma}\left(K_{\mathrm{S}}\frac{\partial S}{\partial \sigma}\right), \tag{30}$$

$$\frac{\partial E}{\partial t}+\frac{u}{L_x}\frac{\partial E}{\partial \chi}+\omega\frac{\partial E}{\partial \sigma}=\frac{K_{\mathrm{M}}}{H^2}\left[\left(\frac{\partial u}{\partial \sigma}\right)^2+\left(\frac{\partial v}{\partial \sigma}\right)^2\right]+\frac{1}{H^2}\frac{\partial}{\partial \sigma}\left(K_{\mathrm{E}}\frac{\partial E}{\partial \sigma}\right)-\frac{g}{H}\left(\alpha K_{\mathrm{T}}\frac{\partial T}{\partial \sigma}-\delta K_{\mathrm{S}}\frac{\partial S}{\partial \sigma}\right)-\varepsilon, \tag{31}$$

where ω is the 'vertical velocity' in new co-ordinates, defined by

$$\omega=\frac{D\sigma}{Dt}=\frac{\partial \sigma}{\partial t}+\frac{u}{L_x}\frac{\partial \sigma}{\partial \chi}+w\frac{\partial \sigma}{\partial z}; \tag{32}$$

ω may be obtained diagnostically, by integrating (28a) vertically using (28b) and the boundary condition $\omega=0$ at $\sigma=0$, as

$$H\omega=\frac{\sigma}{L_x}\frac{\partial}{\partial \chi}(H\bar{u})-\frac{1}{L_x}\frac{\partial}{\partial \chi}\int_0^{\sigma}(Hu)\,\mathrm{d}\sigma. \tag{33}$$

The boundary conditions (15) and (16) become: (i) at the sea surface $\sigma=1$,

$$\omega=0, \tag{34a}$$

$$\frac{K_{\mathrm{M}}}{H}\frac{\partial u}{\partial \sigma}=\frac{\tau_x^{\zeta}}{\rho_0}, \qquad \frac{K_{\mathrm{M}}}{H}\frac{\partial v}{\partial \sigma}=\frac{\tau_y^{\zeta}}{\rho_0}, \tag{34b, c}$$

$$\frac{\partial T}{\partial \sigma}=\frac{\partial S}{\partial \sigma}=\frac{\partial E}{\partial \sigma}=0; \tag{34d}$$

(ii) at the sea floor $\sigma=0$,

$$u=v=0, \tag{35a}$$

$$\frac{\partial T}{\partial \sigma}=\frac{\partial S}{\partial \sigma}=\frac{\partial E}{\partial \sigma}=0, \tag{35b}$$

$$\omega=0. \tag{35c}$$

The forms of the boundary conditions at the western and eastern boundaries are unaltered. Finally, the length scales given in (12a,b) are written as

$$\lambda_1=\kappa[z_{0\mathrm{s}}+(1-\sigma)H], \qquad \lambda_2=\kappa(z_{0\mathrm{b}}+\sigma H). \tag{36a, b}$$

Adding (28a) into (26), (27) and (29)–(31), a set of equations in flux form which have conservation characteristics may be obtained as

$$\begin{aligned}\frac{\partial \mathsf{u}}{\partial t}+\frac{1}{L_x}\frac{\partial}{\partial \chi}(u\mathsf{u})+\frac{\partial}{\partial \sigma}(\omega \mathsf{u})-f\mathsf{v}={}&-\frac{gH}{L_x}\frac{\partial \zeta}{\partial \chi}+gH\alpha\left\{\int_0^1 \frac{1}{L_x}\frac{\partial \mathsf{T}}{\partial \chi}\,\mathrm{d}\sigma-\frac{1}{L_x}\left[\frac{\partial \zeta}{\partial \chi}T_{\sigma=1}+\left(\frac{\partial h}{\partial \chi}-\sigma\frac{\partial H}{\partial \chi}\right)T\right]\right\}\\&-gH\delta\left\{\int_0^1 1_x/k_x\frac{\partial \mathsf{S}}{\partial \chi}\,\mathrm{d}\sigma-\frac{1}{L_x}\left[\frac{\partial \zeta}{\partial \chi}S_{\sigma=1}+\left(\frac{\partial h}{\partial \chi}-\sigma\frac{\partial H}{\partial \chi}\right)S\right]\right\}\\&+\frac{1}{H^2}\frac{\partial}{\partial \sigma}\left(K_M\frac{\partial \mathsf{u}}{\partial \sigma}\right),\end{aligned}\tag{37}$$

$$\frac{\partial \mathsf{v}}{\partial t}+\frac{1}{L_x}\frac{\partial}{\partial \chi}(u\mathsf{v})+\frac{\partial}{\partial \sigma}(\omega \mathsf{v})+f\mathsf{u}=\frac{1}{H^2}\frac{\partial}{\partial \sigma}\left(K_{\mathrm{M}}\frac{\partial \mathsf{v}}{\partial \sigma}\right),\tag{38}$$

$$\frac{\partial \mathsf{T}}{\partial t}+\frac{1}{L_x}\frac{\partial}{\partial \chi}(u\mathsf{T})+\frac{\partial}{\partial \sigma}(\omega \mathsf{T})=\frac{1}{H^2}\frac{\partial}{\partial \sigma}\left(K_{\mathrm{T}}\frac{\partial \mathsf{T}}{\partial \sigma}\right),\tag{39}$$

$$\frac{\partial \mathsf{S}}{\partial t}+\frac{1}{L_x}\frac{\partial}{\partial \chi}(u\mathsf{S})+\frac{\partial}{\partial \sigma}(\omega \mathsf{S})=\frac{1}{H^2}\frac{\partial}{\partial \sigma}\left(K_{\mathrm{s}}\frac{\partial \mathsf{S}}{\partial \sigma}\right),\tag{40}$$

$$\begin{aligned}\frac{\partial \mathsf{E}}{\partial t}+\frac{1}{L_x}\frac{\partial}{\partial \chi}(u\mathsf{E})+\frac{\partial}{\partial \sigma}(\omega \mathsf{E})={}&\frac{K_{\mathrm{M}}}{H^3}\left[\left(\frac{\partial \mathsf{u}}{\partial \sigma}\right)^2+\left(\frac{\partial \mathsf{v}}{\partial \sigma}\right)^2\right]+\frac{1}{H^2}\frac{\partial}{\partial \sigma}\left(K_{\mathrm{E}}\frac{\partial E}{\partial \sigma}\right)\\&-\frac{g}{H}\left(\alpha K_{\mathrm{T}}\frac{\partial \mathsf{T}}{\partial \sigma}-\delta K_{\mathrm{S}}\frac{\partial \mathsf{S}}{\partial \sigma}\right)-H\varepsilon,\end{aligned}\tag{41}$$

where $\mathsf{u}=Hu$, $\mathsf{v}=Hv$, $\mathsf{T}=HT$, $\mathsf{S}=HS$ and $\mathsf{E}=HE$.

4. FURTHER CO-ORDINATE TRANSFORMATION

Observational evidence[14–16] shows the existence of a logarithmic bottom boundary layer in which the velocity increases logarithmically with the distance from the sea floor. Also, the dynamics of upwelling is dependent on the development of an Ekman layer near the bottom. Hence it is desirable to resolve this high-shear region adequately in the model. To achieve this, the σ-co-ordinate is transformed into a new vertical co-ordinate which leads to fine vertical spacings near the bottom ($\sigma=0$) and surface ($\sigma=1$) in the discretization of the equation.

The new vertical co-ordinate η is defined via

$$\sigma=\sigma_0(\mathrm{e}^{\psi(\eta)}-1),\qquad \psi(\eta)=\eta-\frac{1}{2\eta_{\mathrm{s}}}(1-\sigma_0)\eta^2,\tag{42}$$

where σ_0 is a disposable parameter and η_{s} is the value of η at $\sigma=1$. This enables us to represent the boundary conditions (34b–d) and (35a–c) in such a way that 'flux' can be applied at half-levels, ensuring both conservative characteristics in the numerical scheme and half-levels not far away from the boundaries. This can be seen more explicitly in Section 5. Additionally, fine resolution is also required in the upwelling zone, mainly within the baroclinic Rossby radius of deformation. This is accomplished by a further co-ordinate transformation of the χ-co-ordinate into a new horizontal co-ordinate ξ,

$$\xi=\chi+\theta\ln(1+\chi/\chi_0),\tag{43}$$

where θ and χ_0 are disposable parameters.

Taking (ξ, η, t) as new independent co-ordinates and also writing $\beta(\eta) = \partial\sigma/\partial\eta$ and $F(\chi) = \partial\xi/\partial\chi$, equations (28b), (33) and (37)–(41) become

$$\frac{\partial\zeta}{\partial t} + \frac{F}{L_x}\frac{\partial}{\partial\xi}(H\bar{u}) = 0, \tag{44}$$

$$H\omega = \frac{\sigma F}{L_x}\frac{\partial}{\partial\xi}(H\bar{u}) - \frac{F}{L_x}\frac{\partial}{\partial\xi}\int_0^\eta (u\beta)\,\mathrm{d}\eta, \tag{45}$$

$$\begin{aligned}\frac{\partial u}{\partial t} &+ \frac{F}{L_x}\frac{\partial}{\partial\xi}(uu) + \frac{1}{\beta}\frac{\partial}{\partial\eta}(\omega u) - fv \\ &= -\frac{gHF}{L_x}\frac{\partial\zeta}{\partial\xi} + gH\alpha\left\{\int_0^1 \frac{F\beta}{L_x}\frac{\partial T}{\partial\xi}\,\mathrm{d}\eta - \frac{F}{L_x}\left[\frac{\partial\zeta}{\partial\xi}T_{\sigma=1} + \left(\frac{\partial h}{\partial\xi} - \sigma\frac{\partial H}{\partial\xi}\right)T\right]\right\} \\ &\quad - gH\delta\left\{\int_0^1 \frac{F\beta}{L_x}\frac{\partial S}{\partial\xi}\,\mathrm{d}\eta - \frac{F}{L_x}\left[\frac{\partial\zeta}{\partial\xi}S_{\sigma=1} + \left(\frac{\partial h}{\partial\xi} - \sigma\frac{\partial H}{\partial\xi}\right)S\right]\right\} + \frac{1}{H^2\beta}\frac{\partial}{\partial\eta}\left(K_{\mathrm{M}}\frac{\partial u}{\partial\eta}\right),\end{aligned} \tag{46}$$

$$\frac{\partial v}{\partial t} + \frac{F}{L_x}\frac{\partial}{\partial\xi}(uv) + \frac{1}{\beta}\frac{\partial}{\partial\eta}(\omega v) + fu = \frac{1}{H^2\beta}\frac{\partial}{\partial\eta}\left(\frac{K_{\mathrm{M}}}{\beta}\frac{\partial v}{\partial\eta}\right), \tag{47}$$

$$\frac{\partial T}{\partial t} + \frac{F}{L_x}\frac{\partial}{\partial\xi}(uT) + \frac{1}{\beta}\frac{\partial}{\partial\eta}(\omega T) = \frac{1}{H^2\beta}\frac{\partial}{\partial\eta}\left(\frac{K_{\mathrm{T}}}{\beta}\frac{\partial T}{\partial\eta}\right), \tag{48}$$

$$\frac{\partial S}{\partial t} + \frac{F}{L_x}\frac{\partial}{\partial\xi}(uS) + \frac{1}{\beta}\frac{\partial}{\partial\eta}(\omega S) = \frac{1}{H^2\beta}\frac{\partial}{\partial\eta}\left(\frac{K_{\mathrm{S}}}{\beta}\frac{\partial S}{\partial\eta}\right), \tag{49}$$

$$\begin{aligned}\frac{\partial E}{\partial t} + \frac{F}{L_x}\frac{\partial}{\partial\xi}(uE) + \frac{1}{\beta}\frac{\partial}{\partial\eta}(\omega E) &= \frac{K_{\mathrm{M}}}{H^3\beta^2}\left[\left(\frac{\partial u}{\partial\eta}\right)^2 + \left(\frac{\partial v}{\partial\eta}\right)^2\right] + \frac{1}{H^2\beta}\frac{\partial}{\partial\eta}\left(\frac{K_{\mathrm{E}}}{\beta}\frac{\partial E}{\partial\eta}\right) \\ &\quad - \frac{g}{H}\left(\alpha\frac{K_{\mathrm{T}}}{\beta}\frac{\partial T}{\partial\eta} - \delta\frac{K_{\mathrm{S}}}{\beta}\frac{\partial S}{\partial\eta}\right) - H\varepsilon.\end{aligned} \tag{50}$$

The boundary conditions (34) and (35) become: (i) at the sea surface $\eta = \eta_{\mathrm{s}}$,

$$\omega = 0, \tag{51a}$$

$$\frac{K_{\mathrm{M}}}{H^2\beta}\frac{\partial u}{\partial\eta} = \frac{\tau_x^\zeta}{\rho_0}, \qquad \frac{K_{\mathrm{M}}}{H^2\beta}\frac{\partial v}{\partial\eta} = \frac{\tau_y^\zeta}{\rho_0}, \qquad \frac{\partial T}{\partial\eta} = \frac{\partial S}{\partial\eta} = \frac{\partial E}{\partial\eta} = 0; \tag{51b, c, d}$$

(ii) at the sea floor $\eta = 0$,

$$u = v = 0, \tag{52a}$$

$$\frac{\partial T}{\partial\eta} = \frac{\partial S}{\partial\eta} = \frac{\partial E}{\partial\eta} = 0, \tag{52b}$$

$$\omega = 0. \tag{52c}$$

Equations (44)–(50) together with the corresponding boundary conditions form the final version of the equations used in the numerical model.

To avoid numerical thermal sources and sinks in the analysis region, the integral constraint which governs (48) can be obtained by integrating (48) over the whole analysis region to yield

$$\begin{aligned}\frac{\partial}{\partial t}\int_0^{\eta_s}\int_0^1 \mathsf{T}\,\mathrm{d}\xi\,\mathrm{d}\eta + \int_0^{\eta_1}\int_0^1 \frac{F}{L_x}\frac{\partial}{\partial\xi}(u\mathsf{T})\;\mathrm{d}\xi\,\mathrm{d}\eta + \int_0^{\eta_\mathrm{s}}\int_0^1 \frac{1}{\beta}\frac{\partial}{\partial\eta}(\omega\mathsf{T})\,\mathrm{d}\xi\,\mathrm{d}\eta \\ = \int_0^{\eta_\mathrm{s}}\int_0^1 \frac{1}{H^2\beta}\frac{\partial}{\partial\eta}\left(\frac{K_\mathrm{T}}{\beta}\frac{\partial\mathsf{T}}{\partial\eta}\right)\mathrm{d}\xi\,\mathrm{d}\eta.\end{aligned} \tag{53}$$

Using the boundary conditions (51a), (52c), (51d) and (52b), the third term on the left-hand side and the term on the right-hand side become zero; (53) then reduces to

$$\frac{\partial}{\partial t}\int_0^{\eta_\mathrm{s}}\int_0^1 \mathsf{T}\,\mathrm{d}\xi\,\mathrm{d}\eta + \left(\int_0^{\eta_\mathrm{s}} \frac{F}{L_x}(u\mathsf{T})\,\mathrm{d}\eta\right)_{\xi=0}^{\xi=1} = 0. \tag{54}$$

Since at $\xi = 0, u = 0$, (48) further reduces to

$$\frac{\partial}{\partial t}\int_0^{\eta_\mathrm{s}}\int_0^1 \mathsf{T}\,\mathrm{d}\xi\,\mathrm{d}\eta + \left(\int_0^{\eta_x} \frac{F}{L_x}(u\mathsf{T})\,\mathrm{d}\eta\right)^{\xi=1} = 0. \tag{55}$$

Equation (55) states that change in total thermal energy in the system results solely from the horizontal heat flux across the eastern open-sea boundary $\chi = 1$. The same treatment is also applied to the salinity equation (49) to get

$$\frac{\partial}{\partial t}\int_0^{\eta_\mathrm{s}}\int_0^1 \mathsf{S}\,\mathrm{d}\xi\,\mathrm{d}\eta + \left(\int_0^{\eta_\mathrm{s}} \frac{F}{L_x}(u\mathsf{S})\,\mathrm{d}\eta\right)^{\xi=1} = 0. \tag{56}$$

5. FINITE DIFFERENCE EQUATIONS

The continuous equations are expressed in finite difference form in order to obtain the numerical solution. The horizontal, vertical and time variables ξ, η and t are discretized as

$$\begin{aligned} \xi = \xi_i &= (i-1)\Delta\xi, \quad & i &= 1, 2, \ldots, m, \\ \eta = \eta_k &= (k-1)\Delta\eta, \quad & k &= 1, 2, \ldots, n, \\ t = t_p &= p\Delta t, \quad & p &= 0, 1, 2, \ldots, \end{aligned} \tag{57}$$

where $\Delta\xi = \xi_m/(m-1)$ and $\Delta\eta = \eta_\mathrm{s}/(n-1)$ are the horizontal and vertical grid increments respectively and Δt is the time increment. The value of ξ_m is obtained from (43) by setting $\chi = 1$.

Computations are carried out on a horizontally staggered grid for which two distinct types of computational points are defined. Even points marked by stars are called ζ-points at which ζ, ω, v, S and$T$ are computed, while odd points marked by circles are called u-points at which u, E, λ and $K_\mathrm{M}(K_\mathrm{T}, K_\mathrm{S}, K_\mathrm{E})$ are computed, as illustrated in Figure 2a. An even value is chosen for m such that the coast consists of u-points and the open-sea boundary consists of ζ-points. This staggered grid arrangement is similar to the type-C grid described by Arakawa and Lamb.[16]

An unstaggered grid is used for computations in the vertical. Figure 2b shows the finite difference mesh of the model.

Centred differences are used for the space derivatives in (46), (47) and (50). In the temperature and salinity equations (48) and (49), however, an upstream scheme is used for the horizontal advection terms. Vertical diffusion terms in (46)–(50) and dissipation and suppressive terms in (50) are evaluated by a semi-implicit scheme to guarantee unconditional computational stability with regard to the choice of the vertical grid increment. Forward differences are used for the time stepping. In

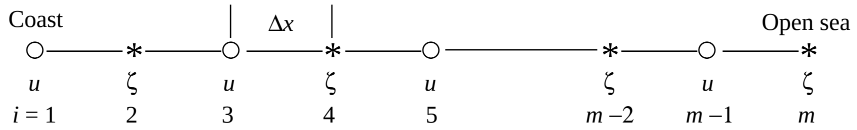

Figure 2a. Staggered grid arrangement in horizontal co-ordinate

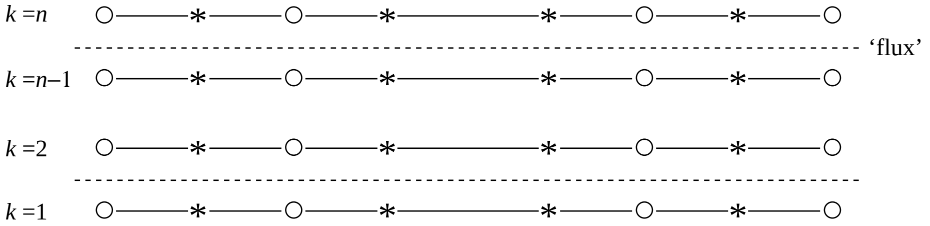

Figure 2b. Finite difference mesh used in model

(43) the value of ξ at each of discrete χ is obtained by the application of a Newton–Raphson iterative procedure. The final form of the finite difference equations (46)–(50) yields a tridiagonal matrix and is solved by a Gaussian elimination method.

The discrete function $F(\xi_i, \eta_k, t_p)$ is denoted by F_i, i.e.

$$F(\xi_i, \eta_k, t_p) = F^p_{i,k} = F_i. \tag{58}$$

Equation (44) is discretized as

$$\frac{\zeta_i^{p+1} - \zeta_i^p}{\Delta t} + \frac{F_i}{L_x}\frac{1}{2\Delta\xi}(\bar{u}^p_{i+1} - \bar{u}^p_{i-1}) = 0 \tag{59}$$

and (58) is used for which ζ is computed at ζ-points $i = 1, 2, 3, \ldots, m-2$. The open-sea radiation condition (18) is applied at $i = m-1$ to compute ζ at $i = m$, which yields

$$\zeta_m^{p+1} = -\zeta_{m-2}^{p+1} + 2\bar{u}^p_{m-1}(h_{m-1}/g)^{1/2}. \tag{60}$$

At the coastline where $i = 1, \zeta$ is determined from extrapolation. The values of ζ at u-points $i = 1, 3, 5, \ldots, m-1$ are then computed by averaging the adjacent updated values of ζ at ζ-points $i = 1, 2, 4, \ldots m$. As a result, values of ζ may be computed at all computational points $i = 1, 2, 3, \ldots, m$.

The finite difference equation corresponding to (45) is

$$H_i^{p+1}\omega_{i,k}^{p+1} = \frac{\sigma_k F_i}{L_x}\frac{1}{2\Delta\xi}(\bar{u}_{i+1} - \bar{u}_{i-1}) - \frac{F_i}{L_x}\frac{1}{2\Delta\xi}\left(\int_0^\eta \beta_k u^p_{i+1,k}\,\mathrm{d}\eta - \int_0^\eta \beta_k u^p_{i-1,k}\,\mathrm{d}\eta\right), \tag{61}$$

where $H_i^{p+1} = \zeta_i^{p+1} + h_i$. Equation (61) is to compute ω at ζ-points $i = 2, 4, \ldots, m-2$ and $k = 2, 3, \ldots, n-1$. The value of ω at $k = 1$ and n are zero from the boundary conditions (51a) and (52c). The values of ω at other points are obtained by averaging or extrapolation from the adjacent updated values of ω.

The discretization of (46) may be written as

$$\frac{\mathsf{u}_{i,k}^{p+1}-\mathsf{u}_{i,k}^{p}}{\Delta t}+\frac{F_i}{L_x}\frac{1}{2\Delta\xi}[(u\mathsf{u})_{i+1,k}^{p}-(u\mathsf{u})_{i-1,k}^{p}]+\frac{1}{\beta_{\mathrm{k}}}\frac{1}{2\Delta\eta}[(\omega\mathsf{u})_{i,k+1}^{p}-(\omega\mathsf{u}_{i,k-1}^{p}]-f\mathsf{v}_{i,k}^{p}$$
$$=-\frac{gH_i^{p+1}F_i}{L_x}\frac{1}{2\Delta\xi}(\zeta_{i+1}^{p+1}-\zeta_{i-1}^{p+1}+g\alpha H_i^{p+1}\left(\int_\sigma^1\frac{F_i}{L_x}\frac{1}{2\Delta\xi}(T_{i+1,k}^{p}-T_{i-1,k}^{p})\beta_k\,\mathrm{d}\eta-\frac{F_i}{L_x}\frac{1}{2\Delta\xi}\right.$$
$$\left.\times[(\zeta_{i+1}^{p+1}-\zeta_{i-1}^{p+1})T_{i,n}^{p}+(h_{i+1}-h_{i-1})T_{i,k}^{p}-\sigma_k(H_{i+1}^{p+1}-H_{i-1}^{p+1})T_{i,k}^{p}]\right)$$
$$-g\delta H_i^{p+1}\left(\int_0^1\frac{F_i}{L_x}\frac{1}{2\Delta\xi}(\mathsf{S}_{i+1,k}^{p}-\mathsf{S}_{i-1,k}^{p})\beta_k\,\mathrm{d}\eta+\frac{F_i}{L_x}\frac{1}{2\Delta\xi}[(\zeta_{i+1}^{p+1}-\zeta_{i-1}^{p+1})S_{i,n}^{p}+(h_{i+1}-h_{i-1})S_{i,k}^{p}\right.$$
$$\left.-\sigma_k(H_{i+1}^{p+1}-H_{i-1}^{p+1})S_{i,k}^{p}]\right)+\frac{1}{(H_i^{p+1})^2\beta_k}\frac{1}{2(\Delta\eta)^2}\left\{\left[\left(\frac{K_{\mathrm{M}}}{\beta}\right)_{i,k+1}^{p}+\left(\frac{K_{\mathrm{M}}}{\beta}\right)_{i,k}^{p}\right]\mathsf{u}_{i,k+1}^{p+1}\right.$$
$$\left.+\left[\left(\frac{K_{\mathrm{M}}}{\beta}\right)_{i,k}^{p}+\left(\frac{K_{\mathrm{M}}}{\beta}\right)_{i,k-1}^{p}\right]\mathsf{u}_{i,k-1}^{p+1}-\left[\left(\frac{K_{\mathrm{M}}}{\beta}\right)_{i,k+1}^{p}+2\left(\frac{K_{\mathrm{M}}}{\beta}\right)_{i,k}^{p}+\left(\frac{K_{\mathrm{M}}}{\beta}\right)_{i,k-1}^{p}\right\}\mathsf{u}_{i,k}^{p+1}\right\}. \tag{62}$$

Rearrangement of (62) gives

$$a_{1,k}\mathsf{u}_{i,k+1}^{p+1}+a_{2,k}\mathsf{u}_{i,k}^{p+1}+a_{3,k}\mathsf{u}_{i,k-1}^{p+1}=a_{4,k}, \tag{63}$$

where $a_{j,k}(j=1,2,3,4)$ are known values.

The boundary condition (51b) is discretized as

$$\frac{1}{(H_i^{p+1})^2}\left(\frac{K_{\mathrm{M}}}{\beta}\right)_{i,n-1/2}^{p}\frac{u_{i,n}^{p+1}-u_{i,n-1}^{p+1}}{\Delta\eta}=\frac{\tau_x^\zeta}{\rho_0}. \tag{64}$$

Hence

$$u_{i,n}^{p+1}=u_{i,n-1}^{p+1}+\frac{2(\tau_x^\zeta/\rho_0)(H_i^{p+1})^2\Delta\eta}{(K_{\mathrm{M}}/\beta)_{i,n}^{p}}+\left(\frac{K_{\mathrm{M}}}{\beta}\right)_{i,n-1}^{p}. \tag{65}$$

The boundary condition (52a) is discretized as

$$u_{i,1}^{p+1}=0. \tag{66}$$

Equation (63) together with (65) and (66) is solved by a Gaussian elimination method for computing the values of u at u-points $i=3,5,\ldots,m-1$ and $k=1,2,\ldots,n$. As mentioned in Section 4, the use of vertical diffusive flux conditions at half-levels leads to the conservation characteristics in the numerical scheme and also accommodates the fact that the vertical grid spacings are very fine near the surface and the bottom. The values of u at u-points $i=3,5,\ldots m-1$ and $k=1,2,\ldots,n$ are then computed as

$$u_{i,k}^{p+1}=\frac{\mathsf{u}_{i,k}^{p+1}}{\zeta_i^{p+1}+h_i}. \tag{67}$$

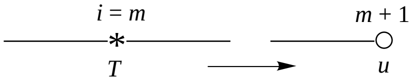

Figure 3a. Horizontal thermal advection at the boundary $i = m$ when $u > 0$

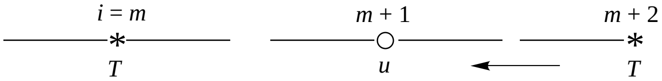

Figure 3b. Horizontal thermal advection at boundary $i = m$ when $u < 0$

Discretizing the y-momentum equation (47) gives

$$\begin{aligned}
&\frac{\mathsf{v}_{i,k}^{p+1} - \mathsf{v}_{i,k}^{p}}{\Delta t} + \frac{F_i}{L_x}\frac{1}{2\Delta\xi}[(u\mathsf{v})_{i+1,k}^{p} - (u\mathsf{v})_{i-1,k}^{p}] + \frac{1}{\beta_k}\frac{1}{2\Delta\eta}[(\omega\mathsf{v})_{i,k+1}^{p} - (\omega\mathsf{v})_{i,k-1}^{p}] + f\,\mathsf{u}_{i,k}^{p+1} \\
&= \frac{1}{(H_i^{p+1})^2\beta_k}\frac{1}{2(\Delta\eta)^2}\left\{\left[\left(\frac{K_{\mathrm{M}}}{\beta}\right)_{i,k+1}^{p} + \left(\frac{K_{\mathrm{M}}}{\beta}\right)_{i,k}^{p}\right]\mathsf{v}_{i,k+1}^{p+1} + \left[\left(\frac{K_{\mathrm{M}}}{\beta}\right)_{i,k}^{p} + \left(\frac{K_{\mathrm{M}}}{\beta}\right)_{i,k-1}^{p}\right]\mathsf{v}_{i,k-1}^{p+1}\right. \\
&\quad \left. - \left[\left(\frac{K_{\mathrm{M}}}{\beta}\right)_{i,k+1}^{p} + 2\left(\frac{K_{\mathrm{M}}}{\beta}\right)_{i,k}^{p} + \left(\frac{K_{\mathrm{M}}}{\beta}\right)_{i,k-1}^{p}\right]\mathsf{v}_{i,k}^{p+1}\right\},
\end{aligned} \tag{68}$$

where the Coriolis force term is evaluated by using the updated values of u to avoid computational instability. The discretization of the boundary conditions (51c) and (52a) is given by

$$\mathsf{v}_{i,n}^{p+1} = \mathsf{v}_{i,n-1}^{p+1} + \frac{2(\tau_y^{\zeta}/\rho_0)(H_i^{p+1})^2\Delta\eta}{(K_{\mathrm{M}}/\beta)_{i,n}^{p} + (K_{\mathrm{M}}/\beta)_{i,n-1}^{p}}, \qquad \mathsf{v}_{i,1}^{p+1} = 0. \tag{69a, b}$$

The values of v at $i = 2, 4, \ldots, m-2$ and $k = 1, 2, \ldots, n$ can be computed from (68), (69a) and (69b) in a similar way as explained for the computation of u. The values of v at ζ-points $i = 2, 4, \ldots, m-2$ and $k = 1, 2, \ldots, n$ are given by

$$v_{i,k}^{p+1} = \frac{\mathsf{v}_{i,k}^{p+1}}{\zeta_i^{p+1} + h_i}.$$

Discretizing the turbulence energy equation (50) results in

$$\begin{aligned}
&\frac{\mathsf{E}_{i,k}^{p+1} - \mathsf{E}_{i,k}^{p}}{\Delta t} + \frac{F_i}{\beta_k}\frac{1}{2\Delta\xi}[(u\mathsf{E})_{i+1,k}^{p} - (u\mathsf{E})_{i-1,k}^{p}] + \frac{1}{\beta_k}\frac{1}{2\Delta\eta}[(\omega\mathsf{E})_{i,k+1}^{p} - (\omega\mathsf{E})_{i,k-1}^{p}] \\
&= \frac{1}{(H_i^{p+1})^3\beta_k}\left(\frac{K_{\mathrm{M}}}{\beta}\right)_{i,k}^{p}\left[\left(\frac{u_{i,k+1}^{p} - u_{i,k-1}^{p}}{2\Delta\eta}\right)^2 + \left(\frac{\mathsf{v}_{i,k+1}^{p} - \mathsf{v}_{i,k-1}^{p}}{2\Delta\eta}\right)^2\right] - \frac{c^{3/4}(\mathsf{E}_{i,k}^{p})^{1/2}}{(H_i^{p+1})^2 l_{i,k}^{p}}\mathsf{E}_{i,k}^{p+1} \\
&\quad + \frac{1}{(H_i^{p+1})^2\beta_k}\frac{1}{2(\Delta\eta)^2}\left\{\left[\left(\frac{K_{\mathrm{E}}}{\beta}\right)_{i,k+1}^{p} + \left(\frac{K_{\mathrm{E}}}{\beta}\right)_{i,k}^{p}\right]E_{i,k+1}^{p+1} + \left[\left(\frac{K_{\mathrm{E}}}{\beta}\right)_{i,k}^{p} + \left(\frac{K_{\mathrm{E}}}{\beta}\right)_{i,k-1}^{p}\right]E_{i,k-1}^{p+1}\right. \\
&\quad \left. - \left[\left(\frac{K_{\mathrm{E}}}{\beta}\right)_{i,k+1}^{p} + 2\left(\frac{K_{\mathrm{E}}}{\beta}\right)_{i,k}^{p} + \left(\frac{K_{\mathrm{E}}}{\beta}\right)_{i,k-1}^{p}\right]E_{i,k}^{p+1}\right\} \\
&\quad - \frac{gc^{1/4}l_{i,k}^{p}}{H_i^{p+1}\beta_k 2\Delta\eta}\left(\frac{\alpha(\mathsf{T}_{i,k+1}^{p} - \mathsf{T}_{i,k-1}^{p}) - \delta(\mathsf{S}_{i,k+1}^{p} - \mathsf{S}_{i,k+1}^{p})}{(\mathsf{E}_{i,k}^{p})^{1/2}}\right)\mathsf{E}_{i,k}^{p+1}.
\end{aligned} \tag{70}$$

The discretization of the boundary conditions may be written as

$$\mathsf{E}_{i,n}^{p+1} = \mathsf{E}_{i,n-1}^{p+1}, \qquad \mathsf{E}_{i,2}^{p+1} = \mathsf{E}_{i,1}^{p+1}. \tag{71a, b}$$

From equation (70) the values of E and E may be obtained at u-points $i = 3, 4, \ldots, m-1$ and $k = 1, 2, \ldots, n$ by a method analogous to that of computing u and v.

Equations (36a) and (36b) are discretized as

$$(\lambda_1)^{p+1}_{i,k} = \kappa[z_{0\mathrm{s}} + (1 - \sigma_k H^{p+1}_i)], \qquad (\lambda_2)^{p+1}_{i,k} = \kappa(z_{0\mathrm{b}} + \sigma_k H^{p+1}_i). \tag{72a, b}$$

Equations (13) and (14) are discretized as

$$(K_{\mathrm{M}})^{p+1}_{i,k} = c^{1/4} l^{p+1}_{i,k} (E^{p+1}_{i,k})^{1/2} + N, \tag{73}$$

$$(K_{\mathrm{D}})^{p+1}_{i,k} = (K_{\mathrm{S}})^{p+1}_{i,k} = (K_{\mathrm{T}})^{p+1}_{i,k} = (K_{\mathrm{E}})^{p+1}_{i,k} = c^{1/4} l^{p+1}_{i,k} (E^{p+1}_{i,k})^{1/2}. \tag{74}$$

The values of $l, K_{\mathrm{T}}, K_{\mathrm{S}}\ (K_{\mathrm{E}})$ and K_{M} at u-points $i = 3, 5, \ldots, m-1$ and $k = 1, 2, \ldots, n$ are computed using (72)–(74).

The finite difference form of (48) is

$$\begin{aligned}
&\frac{\mathsf{T}^{p+1}_{i,k} - \mathsf{T}^{p}_{i,k}}{\Delta t} + \frac{F_i}{L_x}\frac{1}{4\Delta\xi}[(\mathsf{u}^p_{i+1,k} - |\mathsf{u}^p_{i+1,k}|)T^p_{i+2,k} + (u^p_{i+1,k} + |\mathsf{u}^p_{i+1,k}| - \mathsf{u}^p_{i-1,k} + |\mathsf{u}^p_{i-1,k}|)T^p_{i,k} \\
&\quad - (\mathsf{u}^p_{i-1,k} + |\mathsf{u}^p_{i-1,k}|)T^p_{i-2,k}] + \frac{1}{4\beta_k}\frac{1}{\Delta\eta}[(\omega^p_{i,k+1} + \omega^p_{i,k})(\mathsf{T}^p_{i,k+1} + \mathsf{T}^p_{i,k}) \\
&\quad - (\omega^p_{i,k} + \omega^p_{i,k-1})(\mathsf{T}^p_{i,k} + \mathsf{T}^p_{i,k-1})] \\
&\quad = \frac{1}{(H^{p+1}_i)^2\beta_k}\frac{1}{2(\Delta\eta)^2}\left\{\left[\left(\frac{K_{\mathrm{T}}}{\beta}\right)^p_{i,k+1} + \left(\frac{K_{\mathrm{T}}}{\beta}\right)^p_{i,k}\right]T^{p+1}_{i,k+1} + \left[\left(\frac{K_{\mathrm{T}}}{\beta}\right)^p_{i,k} + \left(\frac{K_{\mathrm{T}}}{\beta}\right)^p_{i,k-1}\right]T^{p+1}_{i,k-1}\right. \\
&\quad \left. - \left[\left(\frac{K_{\mathrm{T}}}{\beta}\right)^p_{i,k+1} + 2\left(\frac{K_{\mathrm{T}}}{\beta}\right)^p_{i,k} + \left(\frac{K_{\mathrm{T}}}{\beta}\right)^p_{i,k-1}\right]T^{p+1}_{i,k}\right\}.
\end{aligned} \tag{75}$$

The boundary conditions (51d) and (52b) are discretized as

$$\mathsf{T}^{p+1}_{i,n} = \mathsf{T}^{p+1}_{i,n-1}, \qquad \mathsf{T}^{p+1}_{i,2} = \mathsf{T}^{p+1}_{i,1}. \tag{76a, b}$$

Equation (75) together with (76) is solved by a Gaussian elimination method to obtain the values of T and T at ζ-points $i = 2, 4, \ldots, m-2$ and $k = 1, 2, \ldots, n$.

The discretized form of the salinity equation (49) is

$$\begin{aligned}
&\frac{S^{p+1}_{i,k} - S^{p}_{i,k}}{\Delta t} + \frac{F_i}{L_x}\frac{1}{4\Delta\xi}[(\mathsf{u}^p_{i+1,k} - |\mathsf{u}^p_{i+1,k}|)S^p_{i+2,k} + (\mathsf{u}^p_{i+1,k} + |\mathsf{u}^p_{i+1,k}| - \mathsf{u}^p_{i-1,k} + |\mathsf{u}^p_{i-1,k}|)S^p_{i,k} \\
&\quad - (\mathsf{u}^p_{i-1,k} + |\mathsf{u}^p_{i-1,k}|)S^p_{i-2,k}] + \frac{1}{4\beta_{\mathrm{k}}}\frac{1}{\Delta\eta}[(\omega^p_{i,k+1} + \omega^p_{i,k})(\mathsf{S}^p_{i,k+1} + \mathsf{S}^p_{i,k}) \\
&\quad - (\omega^p_{i,k} + \omega^p_{i,k-1})(\mathsf{S}^p_{i,k} + \mathsf{S}^p_{i,k-1})] \\
&\quad = \frac{1}{(H^{p+1}_i)^2\beta_k}\frac{1}{2(\Delta\eta)^2}\left\{\left[\left(\frac{K_{\mathrm{S}}}{\beta}\right)^p_{i,k+1} + \left(\frac{K_{\mathrm{S}}}{\beta}\right)^p_{i,k}\right]\mathsf{S}^{p+1}_{i,k+1}\right. \\
&\quad + \left[\left(\frac{K_{\mathrm{S}}}{\beta}\right)^p_{i,k} + \left(\frac{K_{\mathrm{S}}}{\beta}\right)^p_{i,k-1}\right]\mathsf{S}^{p}_{i,k-1} \\
&\quad \left. - \left[\left(\frac{K_{\mathrm{S}}}{\beta}\right)^p_{i,k+1} + 2\left(\frac{K_{\mathrm{S}}}{\beta}\right)^p_{i,k} + \left(\frac{K_{\mathrm{S}}}{\beta}\right)^p_{i,k-1}\right]\mathsf{S}^{p+1}_{i,k}\right\}.
\end{aligned} \tag{77}$$

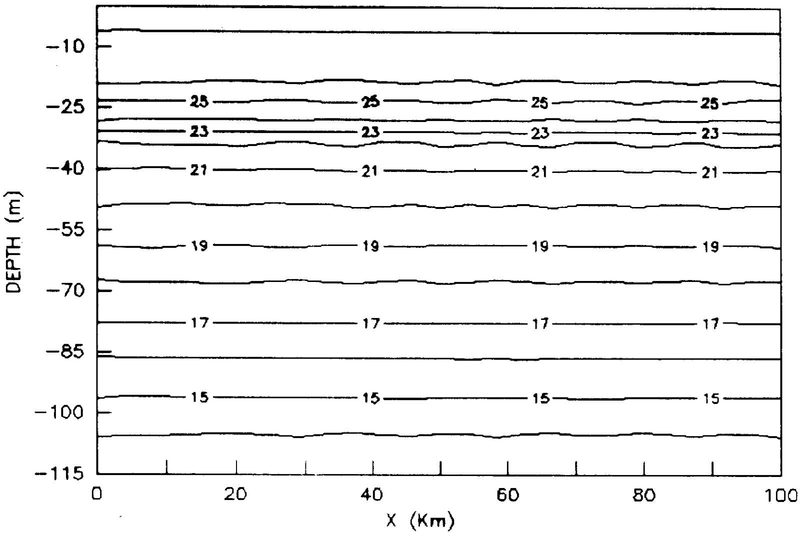

Figure 4a. Initial temperature field

The boundary conditions (51d) and (52b) are discretized as

$$\mathsf{S}^{p+1}_{i,n} = \mathsf{S}^{p+1}_{i,n-1}, \qquad \mathsf{S}^{p+1}_{i,2} = \mathsf{S}^{p+1}_{i,1}. \tag{78a, b}$$

Equation (77) together with (78) is again solved by a Gaussian elimination method to obtain the values of S and S at ζ-points $i = 2, 4, \ldots, m-2$ and $k = 1, 2, \ldots, n$.

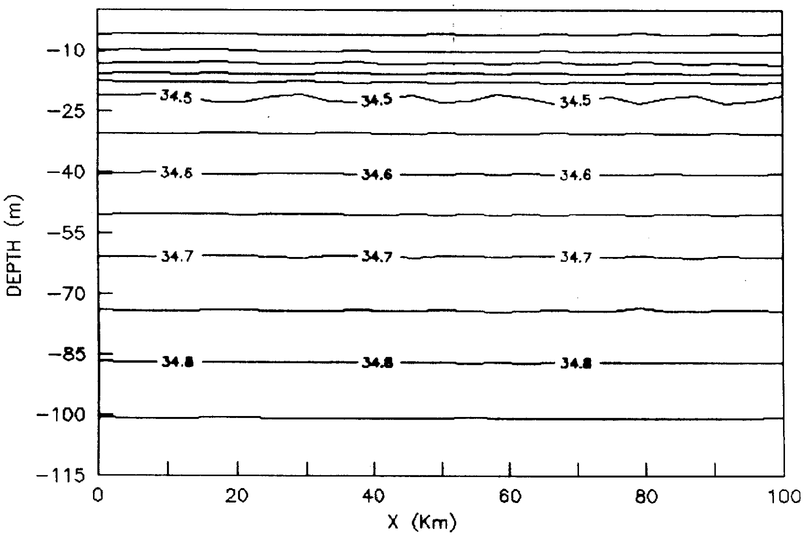

Figure 4b. Initial salinity field

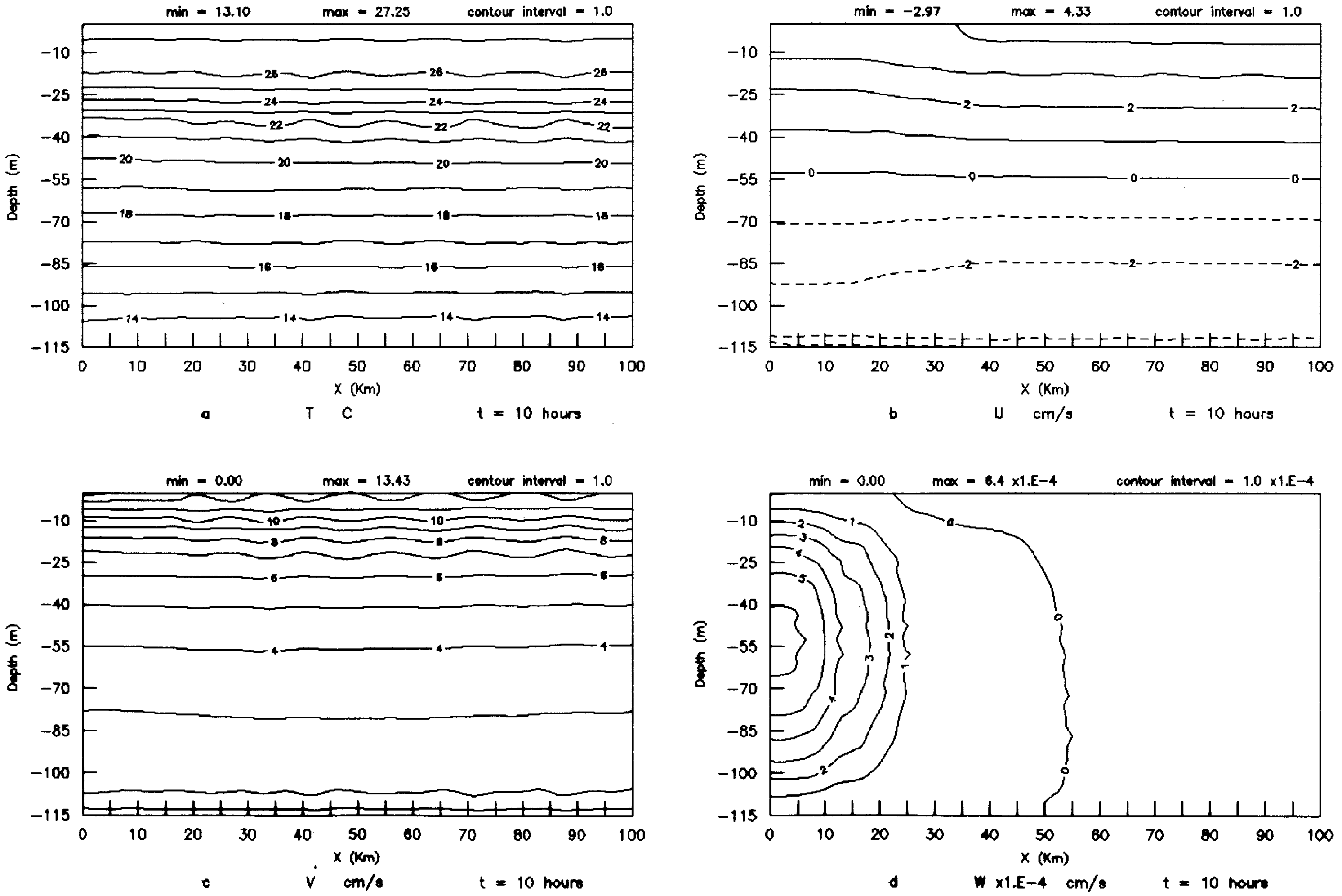

Figure 5. Circulation and temperature field in vertical section normal to coast at 10 h: a, temperature T; b, onshore–offshore velocity u; c, alongshore velocity v; d, vertical velocity w

In (62), (68) and (70) the discretization of the horizontal advection term is neglected near the open-sea boundary ($i = m - 2$ or $m - 1$). However, in (75) the horizontal temperature advection term is obtained at the open-sea boundary ($i = m$) and discretized as

$$\begin{aligned}\frac{F_m}{L_x}\frac{1}{4\Delta\xi}&[(u^p_{m+1,k} - |u^p_{m+1,k}|)T^p_{m+2,k} + (u^p_{m+1,k} + |u^p_{m+1,k}| - u^p_{m-1,k} + |u^p_{m-1,k}|)T^p_{m,k}\\ &- (u^p_{m-1,k} + |u^p_{m-1,k}|)T^p_{m-2,k}],\end{aligned} \tag{79}$$

where $u^p_{m+1,k}$ is obtained by extrapolation and $T^P_{m+2,k}$ is the temperature just outside the open-sea boundary, which is prescribed as temporally invariant. It will be seen that the discretization scheme used in the temperature (48) is consistent with the integral constraint given by equation (55).

The summation of (79) along the horizontal from $i = 2$ to m gives

$$\begin{aligned}2\Delta\xi\sum_{i=2}^{m(2)}\frac{\partial}{\partial\xi}(uT)^p_{i,k} &= \tfrac{1}{2}\sum_{i=2}^{m(2)}[(u^p_{i+1,k} - |u^p_{i+1,k}|)T^p_{i+2,k} + (u^p_{i+1,k} + |u^p_{i+1,k}| - u^p_{i-1,k} + |u^p_{i-1,k}|)T^p_{i,k}\\ &\quad - (u^p_{i-1,k} + |u^p_{i-1,k}|)T^p_{i-2,k}]\\ &= \tfrac{1}{2}[(u^p_{m+1,k} - |u^p_{m+1,k}|)T^p_{m+2,k} + (u^p_{m+1,k} + |u^p_{m+1,k}|)T^p_{m,k}]\\ &\quad - \tfrac{1}{2}[(u^p_{1,k} - |u^p_{1,k}|)T^p_{2,k} + (u^p_{1,k} + |u^p_{1,k}|)T^p_{0,k}],\end{aligned} \tag{80}$$

where the number 2 in parentheses over the summation indicates that the summation over i is carried out with a step of two. The term in the second square brackets in (80) becomes zero owing to the coastal boundary condition $u^p_{1,k} = 0$. Equation (80) is then simplified as

$$2\Delta\xi\sum_{i=2}^{m(2)}\frac{\partial}{\partial\xi}(uT)^p_{i,k} = \tfrac{1}{2}[(u^p_{m+1,k} - |u^p_{m+1,k}|)T^p_{m+2,k} + (u^p_{m+1,k} + |u^p_{m+1,k}|)T^p_{m,k}]. \tag{81}$$

The summation of (75) along the vertical from $k = 2$ to $n - 1$ yields

$$\begin{aligned}2(\Delta\eta)^2\sum_{k=2}^{n-1}\left[\frac{\partial}{\partial\eta}\left(\frac{K_{\mathrm{M}}}{\beta}\frac{\partial T}{\partial\eta}\right)\right]^{p+1}_{i,k} &= 2\sum_{k=2}^{n=1}\left[\left(\frac{K_{\mathrm{M}}}{\beta}\right)^{p+1}_{i,k+1/2}(T^p_{i,k+1} - T^{p+1}_{i,k})\right.\\ &\quad\left. - \left(\frac{K_{\mathrm{M}}}{\beta}\right)^{p+1}_{i,k-\frac{1}{2}}(T^{p+1}_{i,k} - T^{p+1}_{i,k-1})\right]\\ &= \left[\left(\frac{K_{\mathrm{M}}}{\beta}\right)^{p+1}_{i,n} + \left(\frac{K_{\mathrm{M}}}{\beta}\right)^{p+1}_{i,n-1}\right](T^{p+1}_{i,n} - T^{p+1}_{i,n-1})\\ &\quad - \left[\left(\frac{K_{\mathrm{M}}}{\beta}\right)^{p+1}_{i,2} + \left(\frac{K_{\mathrm{M}}}{\beta}\right)^{p+1}_{i,1}\right](T^{p+1}_{i,2} - T^{p+1}_{i,1}).\end{aligned} \tag{82}$$

Using (76), the right-hand side of (82) becomes zero. Mathematically,

$$2(\Delta\eta)^2\sum_{k=2}^{n-1}\left[\frac{\partial}{\partial\eta}\left(\frac{K_{\mathrm{M}}}{\beta}\frac{\partial T}{\partial\eta}\right)\right]^{p+1}_{i,k} = 0. \tag{83}$$

The summation of (75) along the vertical from $k = 2$ to $n - 1$ yields

$$\begin{aligned}\Delta\eta\sum_{k=2}^{n-2}\left(\frac{\partial}{\partial\eta}(\omega T)\right)^p_{i,k} &= (\omega T^p_{i,n-1/2} - (\omega T)^p_{i,3/2} \approx 0\\ &\approx 0.\end{aligned} \tag{84}$$

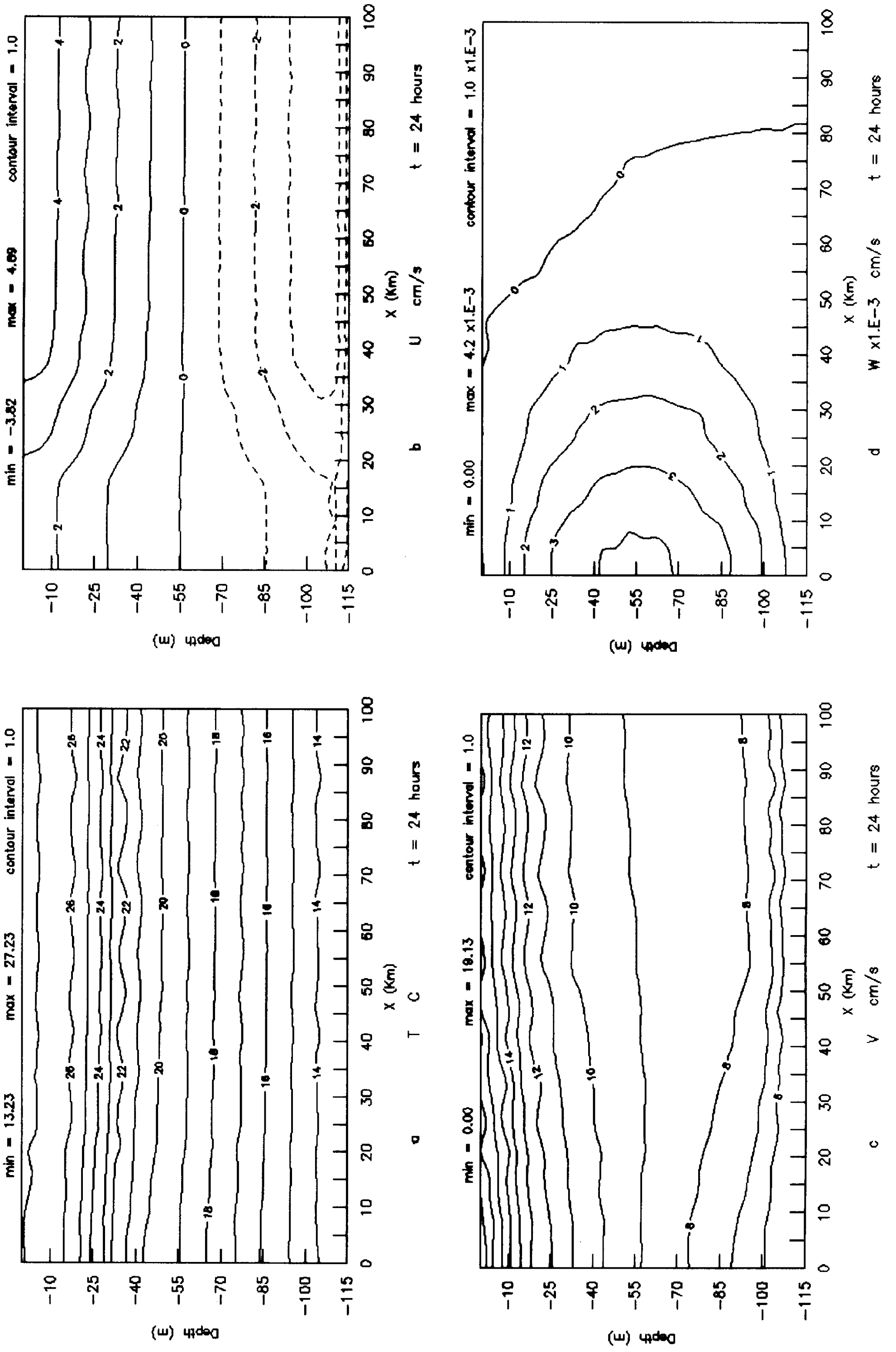

Figure 6. As Figure 5 but at 24 h

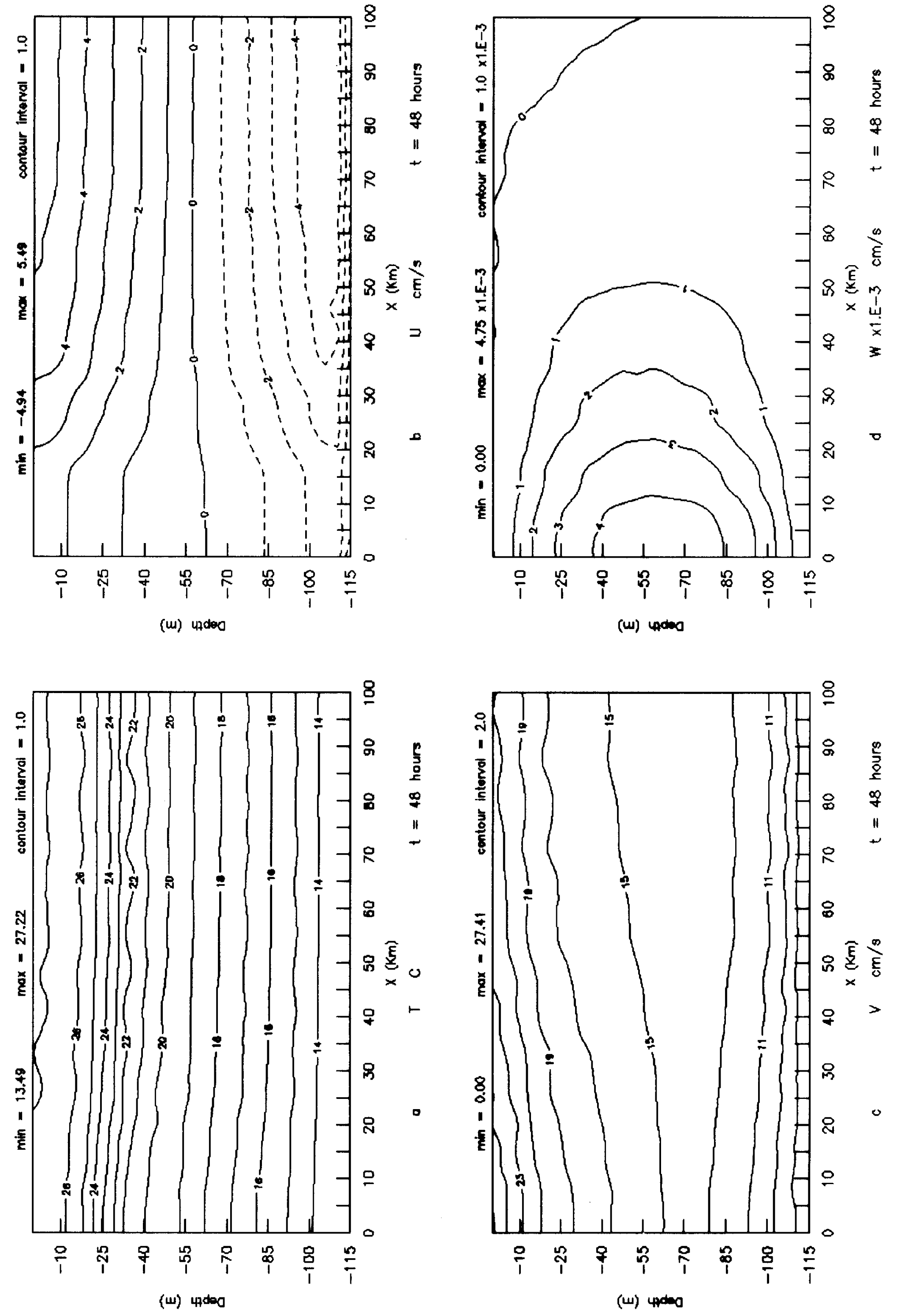

Figure 7. As Figure 5 but at 48 h

Therefore the summation of (75) in both the vertical from $k = 2$ to $n - 1$ and the horizontal from $i = 2$ to m gives

$$\sum_{k=2}^{n} \sum_{i=2}^{m(2)} \frac{T_{i,k}^{p+1} - T_{i,k}^{p}}{\Delta t} \Delta\eta\Delta\xi + \sum_{k=2}^{n} \tfrac{1}{2}[(u_{m+1,k}^{p} - |u_{m+1,k}^{p}|)T_{m+2,k}^{p} + (u_{m+1,k}^{p} + |u_{m+1,k}^{p}|)T_{m,k}^{p}]\Delta\eta = 0. \tag{85}$$

Equation (85) shows that the discretization scheme used in the temperature equation (48) agrees with the integral constraint given by (55). At the same time the horizontal thermal advection at the open boundary is correctly presented.

During outflow, where $u_{m+1,k}^{p}$ is positive, (85) becomes

$$\sum_{k=2}^{n} \sum_{i=2}^{m(2)} \frac{T_{i,k}^{p+1} - T_{i,k}^{p}}{\Delta t} \Delta\eta\Delta\xi + \sum_{k=2}^{n} u_{m+1,k}^{p} T_{m,k}^{p} \Delta\eta = 0, \tag{86}$$

so that the horizontal thermal advection at the boundary is calculated by reference to the value of the temperature at the boundary $i = m$, as illustrated in Figure 3a.

During inflow, where $u_{m+1,k}^{p}$ is negative, (83) reduces to

$$\sum_{k=2}^{n} \sum_{i=2}^{m(2)} \frac{T_{i,k}^{p+1} - T_{i,k}^{p}}{\Delta t} \Delta\eta\Delta\xi + \sum_{k=2}^{n} u_{m+1,k}^{p} T_{m+2,k}^{p} \Delta\eta = 0; \tag{87}$$

therefore the horizontal thermal advection at the boundary is determined by the temperature just outside the boundary ($i = m + 2$), as illustrated in Figure 3b.

A similar discussion holds good for (77) for the horizontal salinity advection at the open-sea boundary $i = m$.

6. NUMERICAL EXPERIMENTS

6.1. Introduction

Experiments are described to investigate the effect of bottom topography on the upwelling and the effect of pure wind stress forcing. To accomplish the latter, a mean monthly wind stress is derived from the wind obtained from the *Climate Atlas of the Indian Ocean*[17] for the month of May in which the upwelling is predominant along the east coast of India. The wind stress derived from the wind is used to drive the model, with which two experiments are performed to understand the dynamics of the upwelling as well as the effect of topography on the upwelling.

The values of several parameters used in the numerical experiments remain unchanged; these parameters and their values are listed in Table I. The grid spacing is uniform in the stretched co-ordinate system but varies non-uniformly in the Cartesian co-ordinates to give fine resolution near the sea floor and the coast. Thus along the x-direction the first grid point is about 1·7 km from the coastline and the grid spacing increases to about 6 km near the open-sea boundary. In the vertical direction 36 levels have been chosen, with resolution about 10 m in the deep region and of the order of 1 cm at the sea bed. In the more shallow coastal upwelling regions (Experiment 2) the resolution at the sea bed is of the order of only 0·2 cm because of the local depth. A time increment of 90 s is found to give computational stability on the basis of CFL criteria and is used in these experiments.

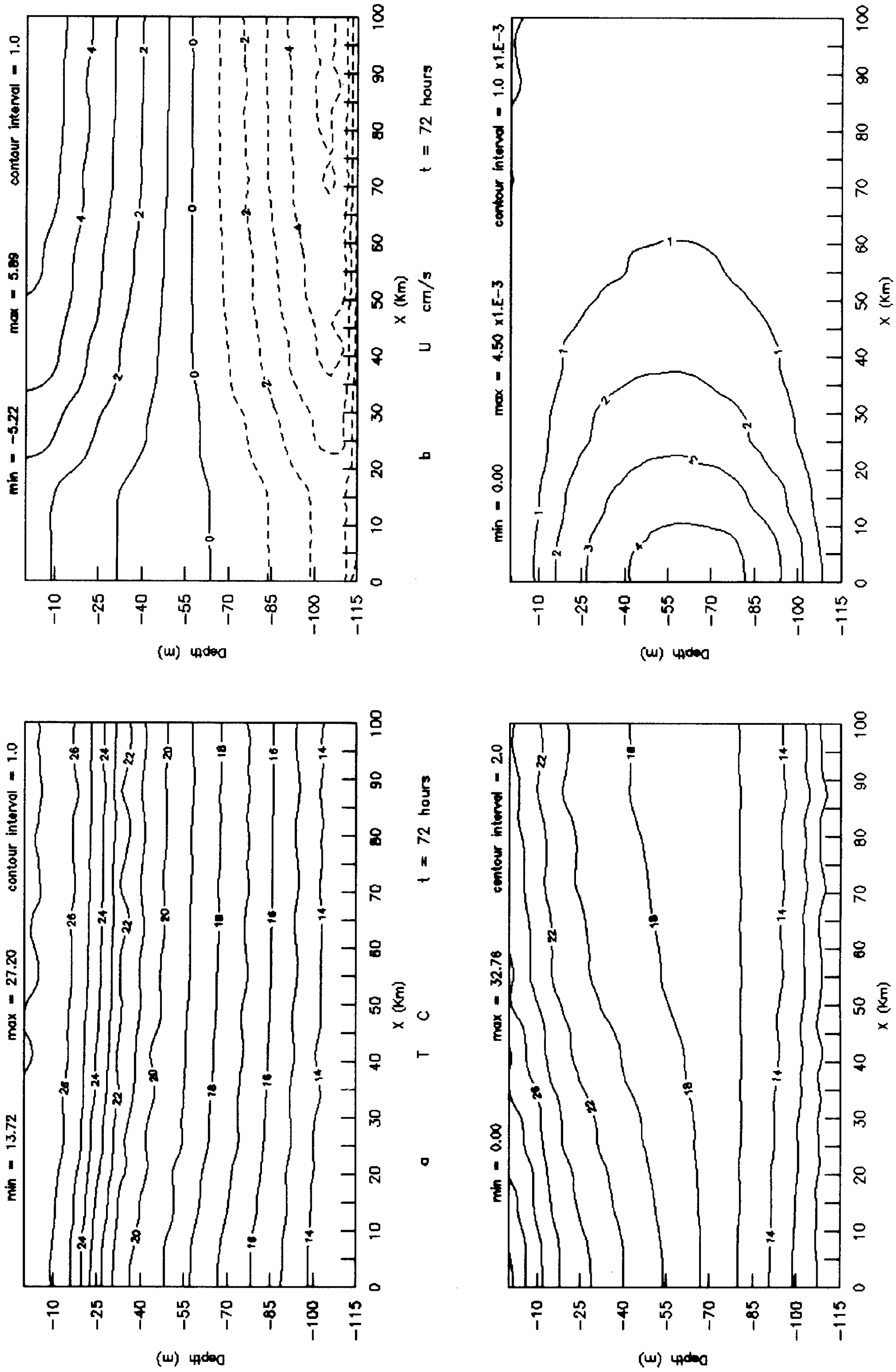

Figure 8. As Figure 5 but at 72 h

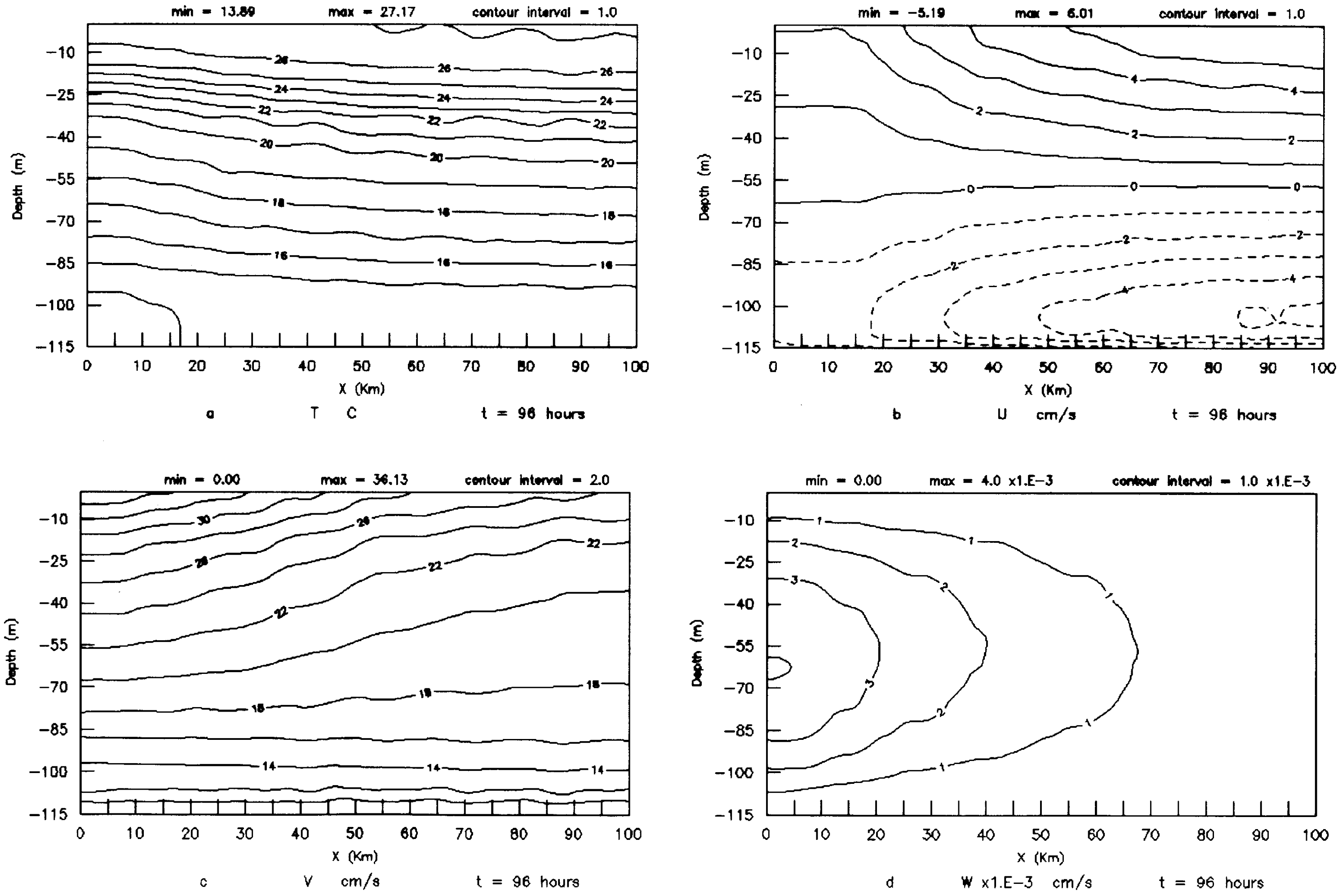

Figure 9. As Figure 5 but at 96 h

Table I. Fixed parameters of numerical calculation

Parameter	Value	Description
L_x	100 km	Horizontal length
m	20	Number of horizontal grid points
n	36	Number of vertical grid points
Z_{ob}	0·01 m	Bottom roughness
$Z_{0\mathrm{S}}$	10·0 m	Surface roughness
γ	0·8	Disposable parameter
σ_0	0·0001	Disposable parameter
θ	0·04	Disposable parameter
χ_0	0·004	Disposable parameter

6.2. *Experiment 1. Flat bottom case*

This experiment is carried out with a constant water depth of 115 m. The fluid is assumed to be initially at rest. A spatially uniform alongshore wind stress $\tau_y = 0{\cdot}03$ N m^{-2}, which corresponds to a northerly wind with a speed of 5 ms^{-1} at 10 m above the sea surface, is imposed at time $t = 0$ and held constant for the entire duration of the integration. The initial temperature and salinity distributions have no horizontal variations but only a uniform vertical gradient (Figure 4). The temperature just outside the open-sea boundary is considered as equal to the temperature at the open-sea boundary ($T_{m+2,k} = T_{m,k}$) and is assumed to be temporally invariant during the integration. In a similar fashion the salinity at the open-sea boundary is taken ($S_{m+2,k} = S_{m,k}$).

6.2.1. Circulation and thermal structure. Figure 5a shows the thermal structure at time $t = 10$ h. The contours are drawn at an interval of $\Delta T = 1$ °C. As observed, there is no significant effect of surface wind stress on the thermal structure. The 26 °C isotherm is horizontal without any unwarping. Figure 5b shows the effect of impulsive application of alongshore wind stress in generating an offshore flow near the surface and with a thickness of nearly 55 km. In the bottom layers a compensating onshore flow exists to satisfy the law of conservation of mass. As an initial response to the wind stress forcing, the offshore flow is substantial, 4·3 cm s^{-1}, with an onshore flow of 3 cm s^{-1}. Figure 5c shows the alongshore velocity, which is in the same direction as the applied wind stress τ_y^{ζ} at all depths. The value of v increases from the bottom to the surface from 1 to 13 cm s^{-1}. There is a very narrow coastal jet near the surface, which corresponds to a weak horizontal temperature gradient (Figure 5a). The vertical velocity plotted in Figure 5d shows upwelling appearing near the coast, with a maximum of $0{\cdot}6 \times 10^{-3}$ cm s^{-1} appearing at a depth of 55 m.

The circulation and thermal structure at $t = 24$ h are shown in Figure 6. The results indicate that the upwelling process has started and the characteristics are slowly unfolding, but the response is still at an early stage. From Figure 6b we can see that there is a strong vertical shear in the surface layers and the bottom Ekman layer is also developed. The maximum onshore flow is 3·8 cm s^{-1}, which occurs at 110 m depth. The onshore velocity decreases uniformly to 55 m depth, after which the offshore velocity starts increasing towards the surface. Examination of Figure 6d shows that the upwelling takes place within 40 km of the coast, which is equivalent to the baroclinic radius of deformation, Nh/f, where N is the Brunt–Väsäla frequency. The maximum vertical velocity is $4{\cdot}9 \times 10^{-3}$ cm s^{-1} at 55 m depth and is found to be increased in magnitude compared with the 10 h result. The thermal structure in Figure 6a shows an upward tilt of the isotherms near the coast, whereas the isotherms are horizontal away from the coast. This upwarping near the coast indicates that cold water from the bottom is moving upwards owing to upwelling. The thermal advection and

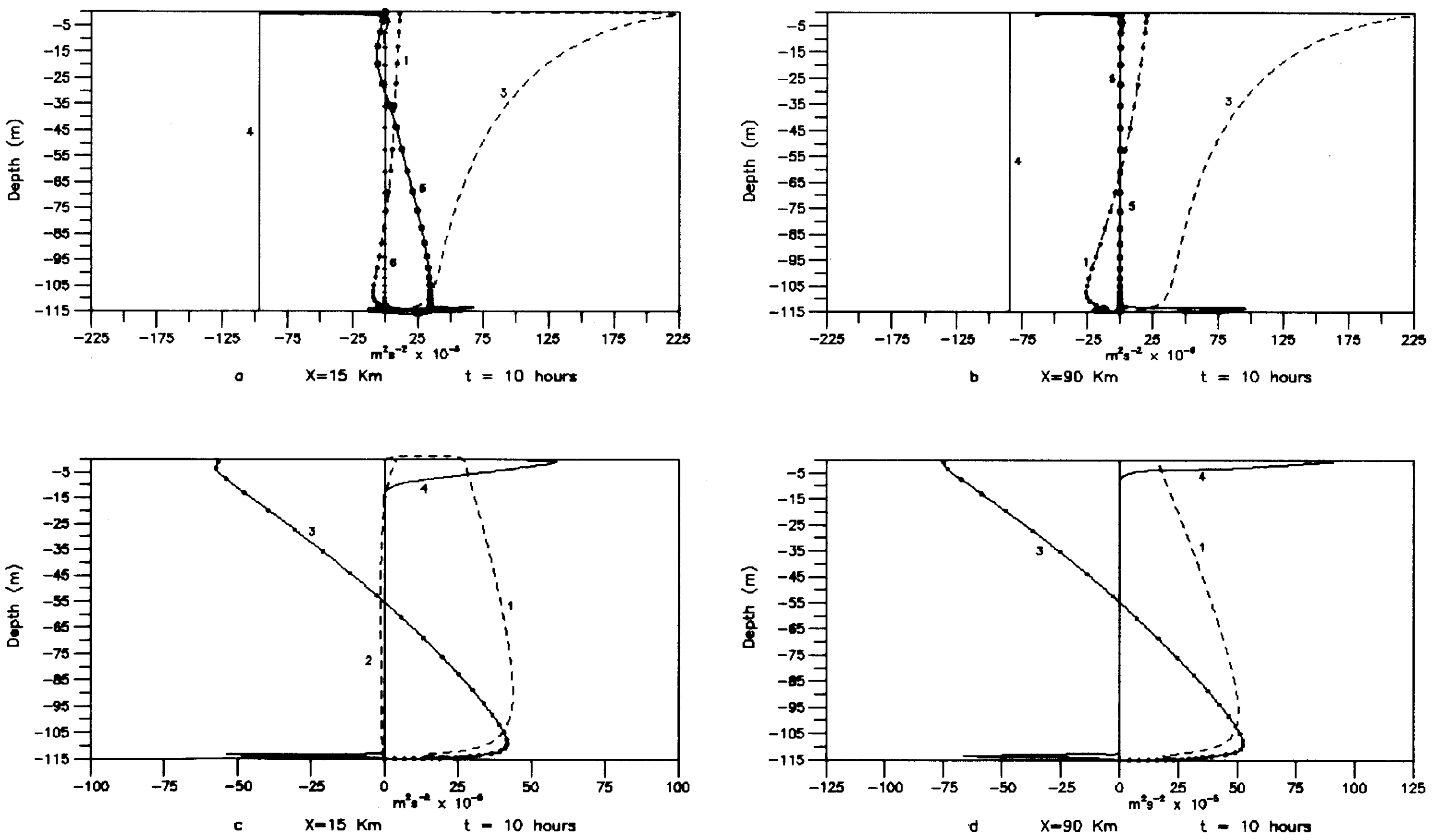

Figure 10. Vertical distribution at 10 h of terms in *x*-momentum equation at (a) 15 km and (b) 90 km offshore and in *y*-momentum equation at (c) 15 km and (d) 90 km offshore

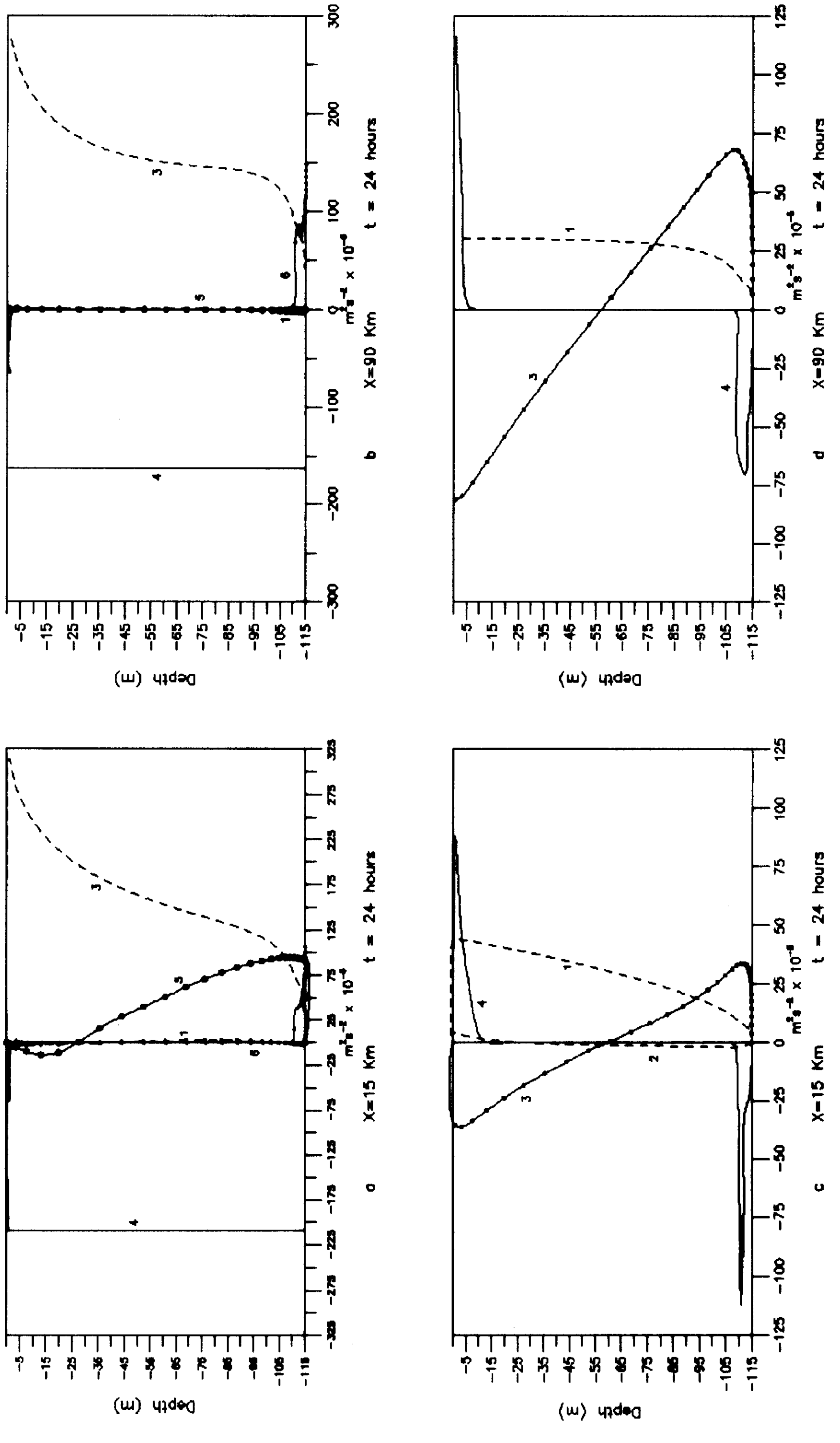

Figure 11. As Figure 10 but at 24 h

diffusion processes as per the temperature equation (6) lead to the intersection of the 27 °C isotherm with the surface near the coast. The surface mixed layer depth is found to be 15 m. The strong onshore flow near the bottom results in a bottom mixed layer depth of 10 m. Figure 6c reveals that although the alongshore flow is in the direction of τ_y^ζ at all depths, its magnitude near the coast is very different from that in the seaward region at the same level. The narrow baroclinic coastal jet has developed near the surface with a maximum velocity of 19 cm s^{-1}. However, in the seaward region the maximum alongshire velocity is only 16 cm s^{-1} and also there is no horizontal shear as a consequence of the spatial uniformity of the wind stress and the absence of the horizontal thermal gradient.

The development of the baroclinic coastal jet can be interpreted as follows. The upward tilt of the isotherms near the coast implies that the baroclinic pressure gradient points offshore and increases in magnitude with depth. Alternatively, we can say that it is actually in the opposite direction to the gradient of the sea surface elevation. Thus, the onshore–offshore velocity is reduced near the coast compared with that in the seaward region where the horizontal temperature gradient is absent. The reduction in the onshore–offshore velocity (increase in Coriolis force in the y-momentum equation) in turn requires an increased alongshore flow near the surface (the baroclinic coastal jet). The development of the coastal jet is therefore associated with the evolution of the horizontal temperature gradient in the region.

Examination of Figure 7, which gives the flow fields and thermal structure at $t = 48$ h, indicates further intensification of the upwelling. From Figure 7b it is found that the maximum offshore velocity is 5·5 cm s^{-1}; at the same time the onshore velocity is also strengthened to 4·5 cm s^{-1}. The surface layer of offshore velocity is about 60 m and also the strength of the new onshore flow decreases more rapidly above the bottom layers as required by mass conservation. A closer examination shows that the bottom mixed layer has increased slightly to 20 m in depth. Figure 7d shows that the upwelling is now extended to 50 km offshore and the maximum lies at about 60 m depth with a value of $4{\cdot}75 \times 10^{-3}$ cm s^{-1}. It seems that as time progresses, the vertical position of maximum vertical velocity is occurring at greater depths, which in fact coincides with the location of zero offshore flow. Figure 7a gives the thermal structure, which reveals that near the shore the isotherms have greater upward tilts. This is consistent with the fact that there is rising cold water in this zone, as is evident from Figure 7d. The isotherms are horizontal in the seaward region but slowly show an upward tilt, finally resulting in intersection with the free surface near the coast. There is no indication of frontal zone formation as reported by Li[10] in his simulations. The surface layer has increased to 15 m in depth and a bottom mixed layer of the same size is formed. Figure 7c shows the alongshore velocity structure with a broader and deeper structured baroclinic coastal jet and strengthened to a maximum value of 27 cm s^{-1}.

Figure 8 gives the circulation and thermal structure of the upwelling at $t = 72$ h. It can be seen from Figure 8b that the offshore flow takes place from the surface to a depth of 60 m with a maximum value of 5·8 cm s^{-1}. The maximum onshore velocity has a value of 5·2 cm s^{-1}. The strong vertical shear near the bottom indicates that the bottom Ekman layer is now well-established. From Figure 8d we can note that the upwelling extends to a greater distance from the coast, about 55 km. The maximum vertical velocity occurs at 65 m depth with a value of $4{\cdot}5 \times 10^{-3}$ cm s^{-1}. The alongshore velocity field (Figure 8c) shows that the baroclinic coastal jet continues to intensify in strength and acquires a maximum value of 32·7 cm s^{-1}. From the thermal structure (Figure 8a) it can be seen that the 27 °C isotherm has migrated further offshore to a distance of 45 km. The horizontal temperature gradient has increased, indicating greater upwarping of the isotherms near the coast. As the cold upwelled water near the surface migrates offshore, the maximum of non-linearities resulting from the horizontal thermal advection is therefore evident. The surface mixed layer has a depth of

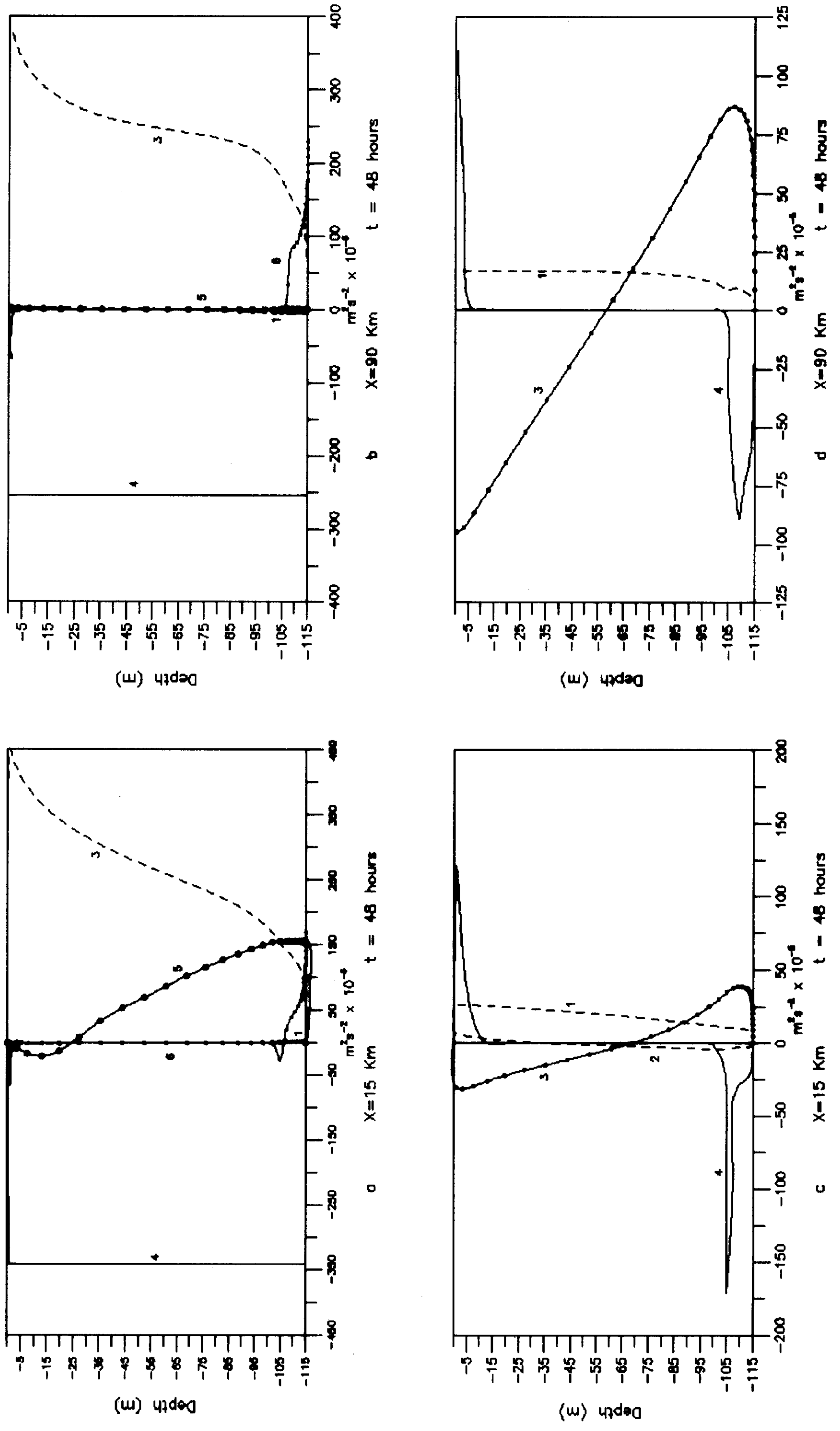

Figure 12. As Figure 10 but at 48 h

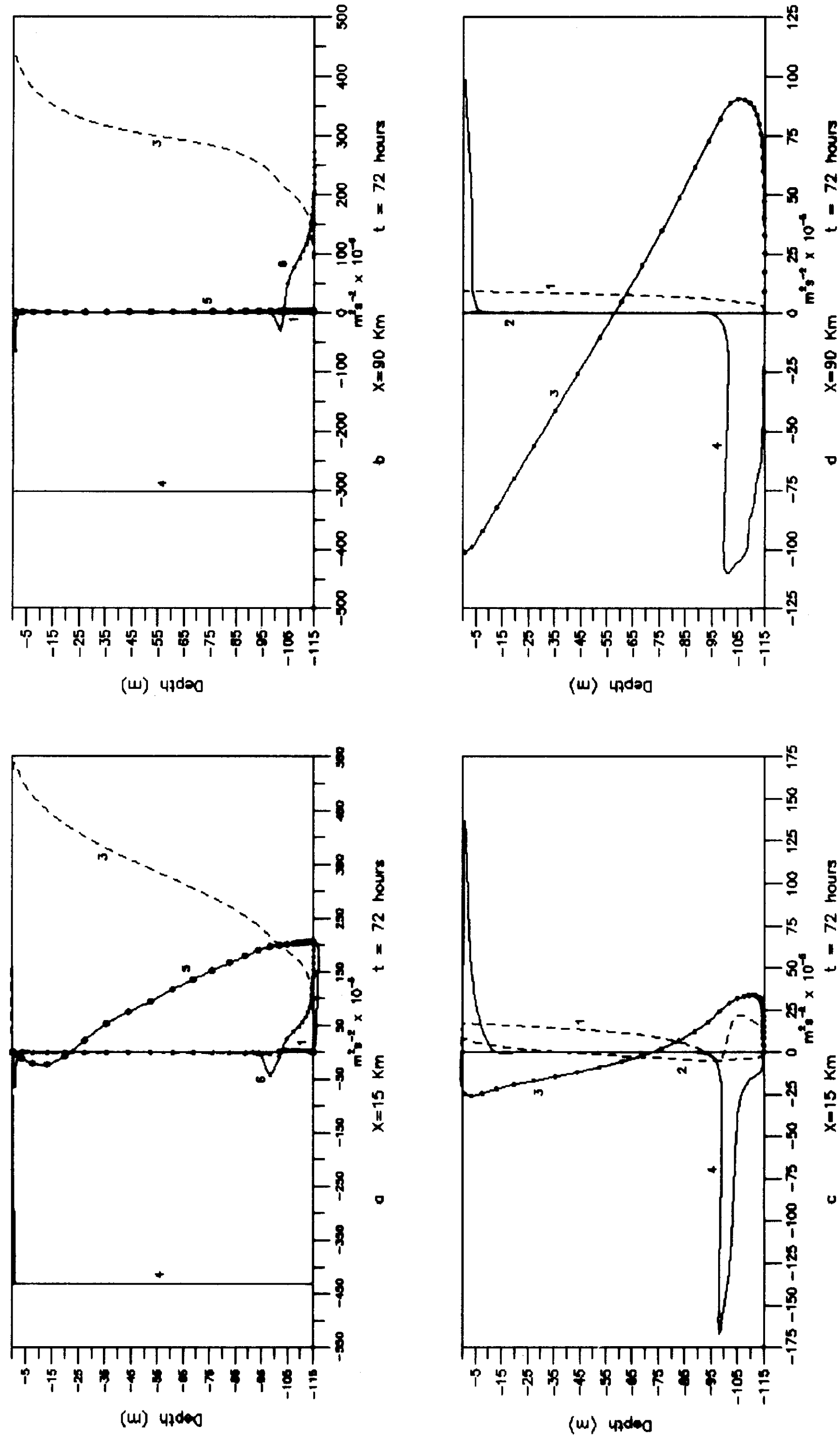

Figure 13. As Figure 10 but at 72 h

15 m and the depth of the bottom layer near the coast is greater than that in the seaward region, which results from the onshore and vertical advection in the bottom mixed layer and in the water column near the coast.

At $t = 96$ h the thermal and flow field structures are as given in Figure 9. The onshore–offshore velocity structure in Figure 9b shows no significant changes in comparison with that at $t = 72$ h. The vertical velocity structure (Figure 9d) shows some weakening and the maximum value occurs at 65 m depth with a magnitude of $4{\cdot}0 \times 10^{-3}$ cm s^{-1}. The offshore extension of the vertical velocity field increases to 60 km compared with that at $t = 72$ h. The onshore flow, which compensates the upper offshore flow by the requirement of mass conservation, is largely concentrated within the fully developed bottom Ekman layer. The alongshore flow (Figure 9c) shows that the baroclinic coastal jet has increased in strength to 35 cm s^{-1} with a strong vertical shear. The thermal structure in Figure 9a shows that the 27 °C isotherm has further migrated offshore to a distance of 65 km. The bottom mixed layer has deepened further, having a thickness of about 20 m, which is more prominently seen here.

The offshore advection in the upper layers leads to a reduction in the thermal content in the analysis area. It is obvious that this cannot be compensated by the onshore thermal advection in the lower layers across the open-sea boundary. As there are no additional dynamical and thermodynamical processes, such as solar radiational heating at the surface, the system cannot be restored to its initial state. As a result, the integration cannot be carried out for a longer time.

6.2.2. Balance analysis. A diagnostic analysis of the various terms in the momentum equations is carried out to investigate the structural features of the upwelling. The various terms in the x-momentum equation (46) are identified as follows:

$$
\begin{aligned}
\underbrace{\frac{\partial u}{\partial t}}_{1} &= \underbrace{-\frac{F}{L_x}\frac{\partial}{\partial \xi}(uu) - \frac{1}{\beta}\frac{\partial}{\partial \eta}(\omega u)}_{2} + \underbrace{fv}_{3} - \underbrace{\frac{gHF}{L_x}\frac{\partial \zeta}{\partial \xi}}_{4} \\
&\quad \underbrace{\begin{aligned}&+ gH\alpha\left\{\int_\sigma^1 \frac{F\beta}{L_x}\frac{\partial T}{\partial \xi}\,\mathrm{d}\eta - \frac{F}{L_x}\left[\frac{\partial \zeta}{\partial \xi}T_{\sigma=1} + \left(\frac{\partial h}{\partial \xi} - \sigma\frac{\partial H}{\partial \xi}\right)T\right]\right\} \\
&\qquad - gH\delta\left\{\int_\sigma^1 \frac{F\beta}{L_x}\frac{\partial S}{\partial \xi}\,\mathrm{d}\eta - \frac{F}{L_x}\left[\frac{\partial \zeta}{\partial \xi}S_{\sigma=1} + \left(\frac{\partial h}{\partial \xi} - \sigma\frac{\partial H}{\partial \xi}\right)S\right]\right\}\end{aligned}}_{5} \\
&\quad + \underbrace{\frac{1}{H^2\beta}\frac{\partial}{\partial \eta}\left(\frac{K_{\mathrm{M}}}{\beta}\frac{\partial u}{\partial \eta}\right)}_{6}. \qquad (88)
\end{aligned}
$$

It is known that the advection term 2 is negligible as its magnitude is generally at least two orders smaller than that of the other terms. Figures 10a and 10b give the vertical distribution of the individual terms in (88) at 10 h; the tendency term 1, the Coriolis term 3, the barotropic pressure gradient term 4, the baroclinic pressure gradient term 5 and the vertical diffusion term 6 at $x = 15$ and 90 km are shown. The region adjacent to $x = 15$ km is considered as representation of the upwelling zone, while the region adjacent to $x = 90$ km is taken as representative of the seaward region.

In the upwelling region (Figure 10a) the vertical diffusion term 6 is only a fraction of the other terms. The balance is effectively achieved between the Coriolis term 3 and the pressure gradient terms 4 and 5. Thus a quasi-geostrophic equilibrium exists in this region. Near the bottom and surface the vertical diffusion term also contributes to the balance. The baroclinic pressure gradient term 5 points offshore and its magnitude increases with depth. The barotropic pressure gradient term 4, on

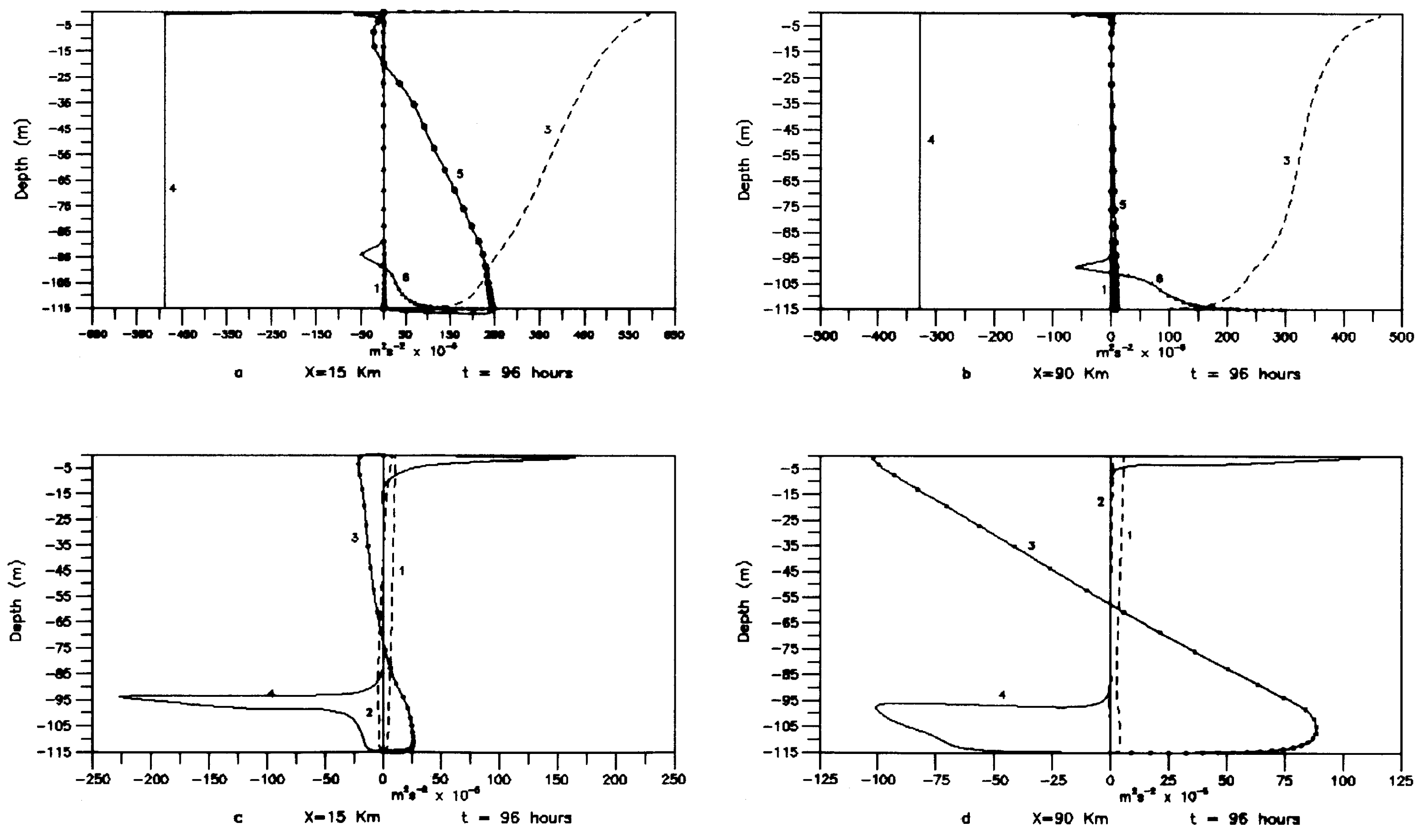

Figure 14. As Figure 10 but at 96 h

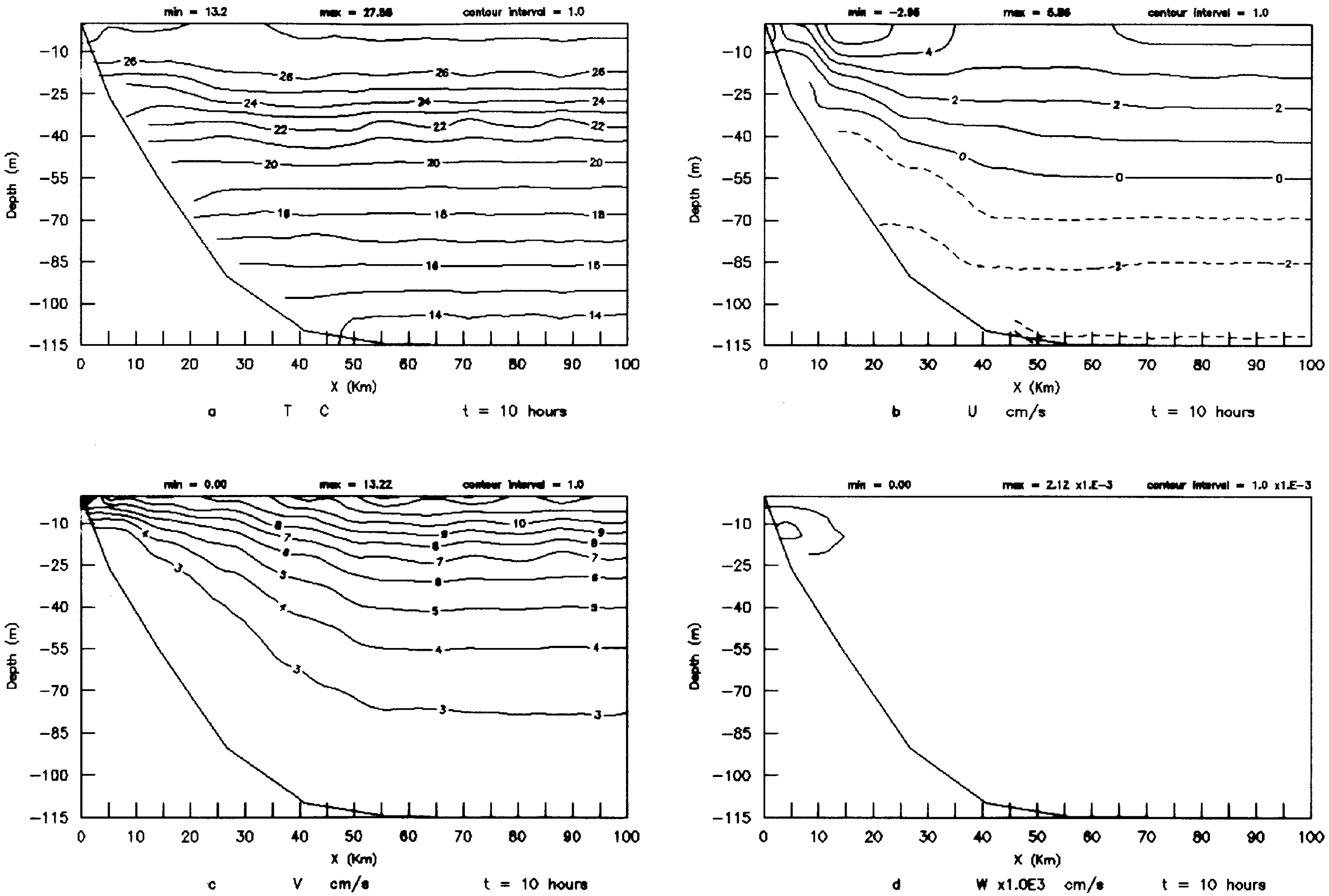

Figure 15. Circulation and temperature field in vertical section normal to coast at 10 h: a, temperature T; b, onshore–offshore velocity u; c, alongshore velocity v; d, vertical velocity w

the other hand, points onshore, with a constant value in the whole water column. Near the surface, where the baroclinic pressure gradient term reduces to zero, an increase in the magnitude of the Coriolis force necessitates a baroclinic coastal jet to maintain the balance of the individual terms in the equation. This shows that the development of the baroclinic coastal jet must be associated with the evolution of the baroclinic pressure gradient term in this region.

In the seaward region (Figure 10b) the vertical diffusion term 6 could be more significant compared with that of the upwelling region. It may play an important role in the balance of the individual terms of the equation, especially in the regions near the surface and bottom. The magnitude of the barotropic pressure gradient terms has decreased in this region, leading to an increase in the magnitude of the tendency term. Also, the baroclinic pressure gradient term 5 is absent, which is in accordance with the absence of the horizontal pressure gradient in the seaward region. As a result, the balance is mainly between the Coriolis force term (3) and the barotropic pressure gradient term 4.

The y-momentum equation (47) may be written similarly to (88) as

$$\underbrace{\frac{\partial v}{\partial t}}_{1} = \underbrace{-\frac{F}{L_x}\frac{\partial}{\partial \xi}(uv) - \frac{1}{\beta}\frac{\partial}{\partial \eta}(\omega v)}_{2} - \underbrace{fu}_{3} + \underbrace{\frac{1}{H^2\beta}\frac{\partial}{\partial \eta}\left(\frac{K_{\mathrm{M}}}{\beta}\frac{\partial v}{\partial \eta}\right)}_{4}. \tag{89}$$

The balance relation in (89) is entirely different from that of (88). Figure 10c reveals the distribution of the individual terms in the upwelling region. By observation it is found that the advection terms are very small. The tendency term 1, resulting from the imbalance of the vertical diffusion term 4 and the Coriolis force term 3, is positive, with a magnitude greater than that in the x-momentum equation. It is also seen that the maximum value of the tendency term has a comparable order of magnitude with the large vertical diffusion term. The large vertical diffusion term results in the rapid intensification of the baroclinic coastal jet.

Figure 10d shows the magnitude of the various terms plotted for the seaward region. Again the advection terms are found to be negligible compared with the other terms 1, 3 and 4. Thus the main balance is between the Coriolis term and the vertical diffusion term. The tendency term is smaller in magnitude compared with that of the upwelling region. Also, it indicates that near the surface the increase in the value of the alongshore velocity is not as large as that of the upwelling region. The fact that the tendency term is positive shows that there is an increase in the alongshore velocity as seen in Section 6.2.1.

Figures 11–14 shows the vertical distribution of the individual terms of the x-momentum equation at 24, 48, 72 and 96 h respectively in the upwelling region (a) and seaward region (b). The balance is achieved in a similar manner to that at 10 h. There exists a balance between the Coriolis force term 3 and the pressure gradient term 4 and 5. The magnitude of the terms 3, 4 and 5 increases as the integration time increases from 24 to 96 h. The baroclinic term has its magnitude of $3{\cdot}5 \times 10^{-4}$ m^2 s^{-2} at $t = 10$ h increased to $2{\cdot}2 \times 10^{-3}$ m^2 s^{-2}, which indicates the intensification of the upwarping of the isotherms near the coast. At the seaward end the main balance is between the Coriolis term and the barotropic pressure gradient term. The vertical diffusion term makes its presence felt by contributing to the balance near the bottom end surface. The baroclinic pressure gradient term is insignificant in magnitude.

For the y-momentum equation the balance is shown in Figures 11–14 at 24, 48, 72 and 96 h respectively. In the upwelling region (c) the magnitude of the individual terms is decreasing. In Figure 12c we can see that the magnitude of the tendency term becomes very small, indicating that the strength of the coastal jet has reached its optimum value in accordance with the balance between

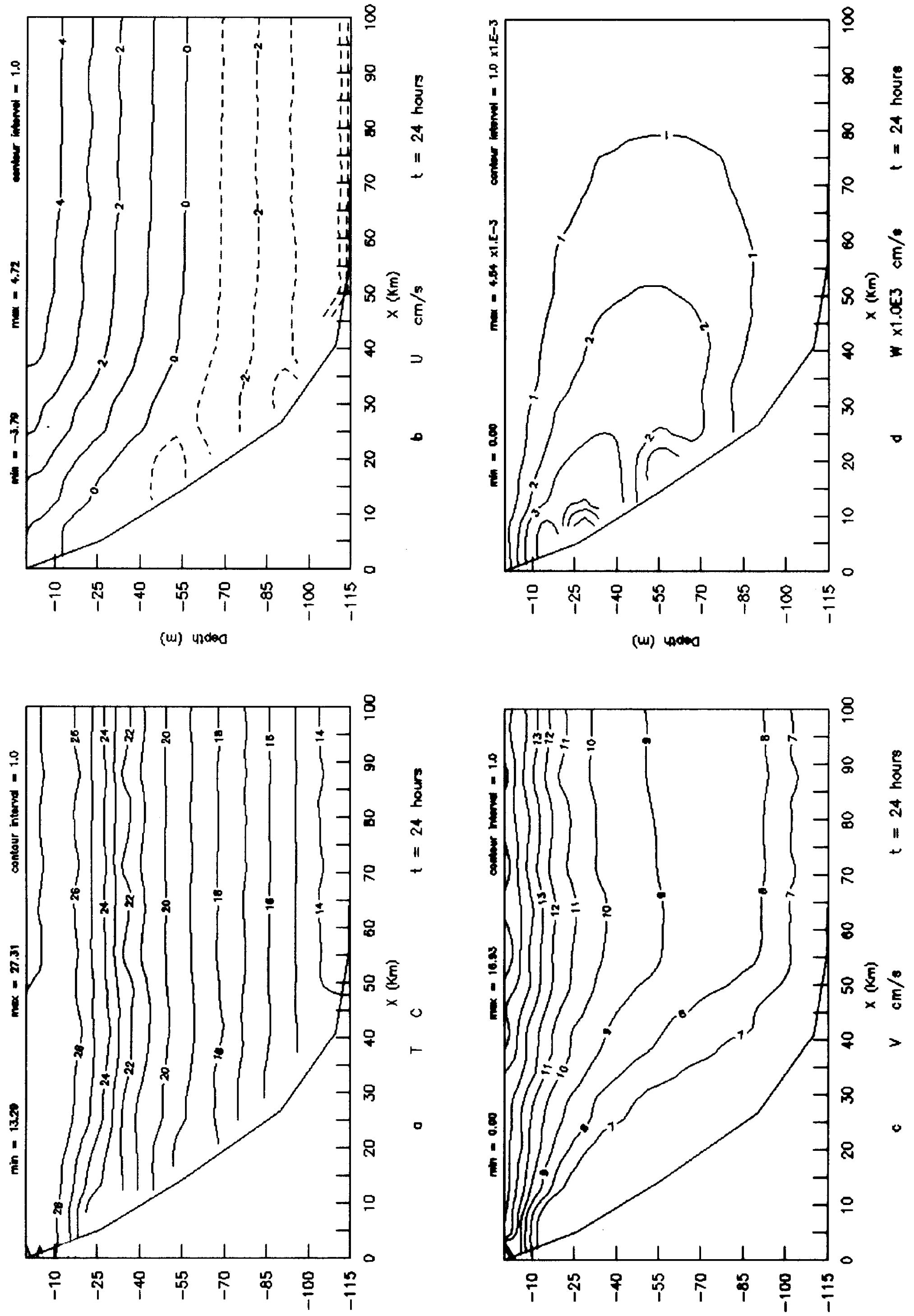

Figure 16. As Figure 15 but at 24 h

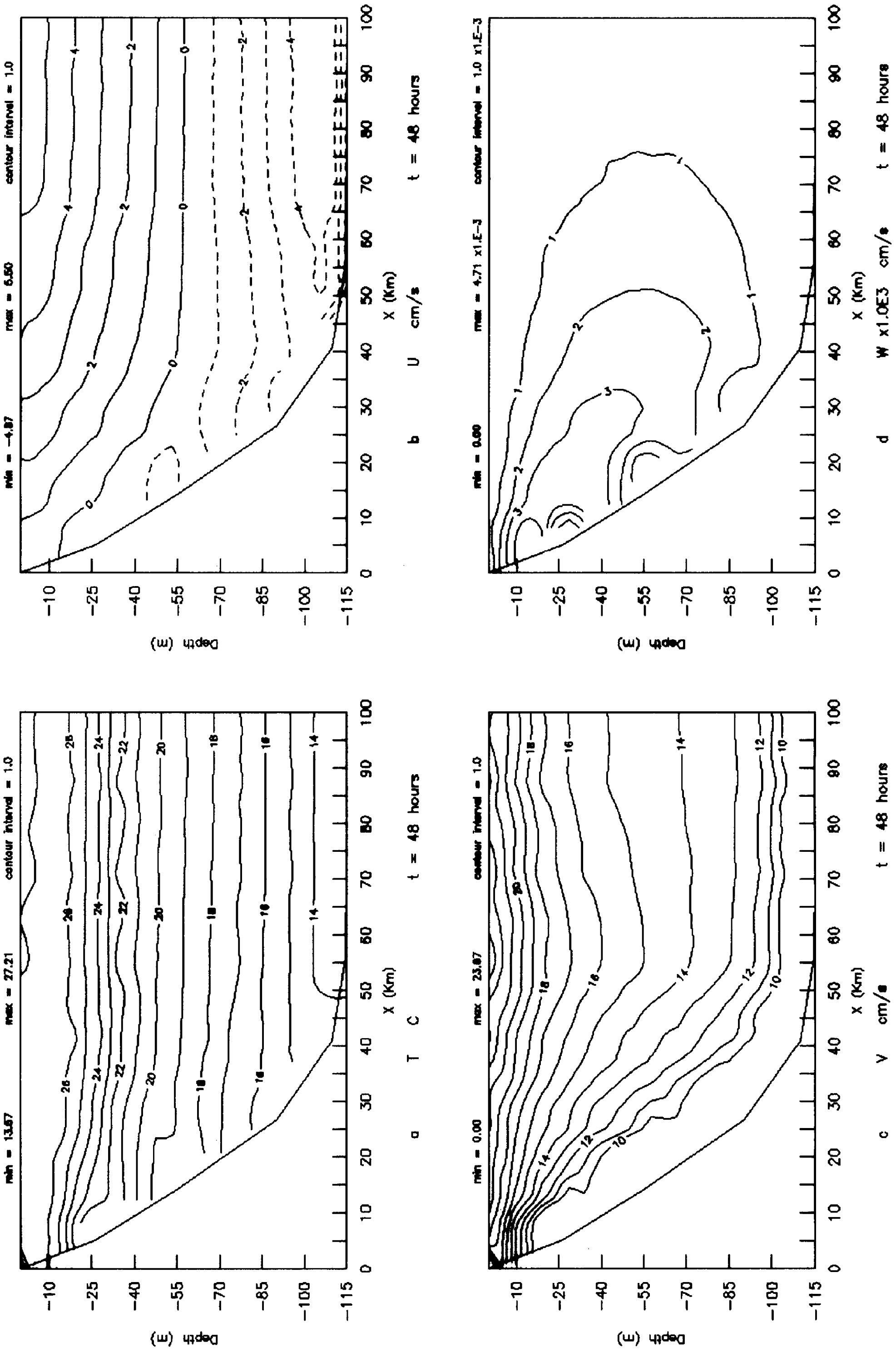

Figure 17. As Figure 15 but at 48 h

the various terms. In the seaward region (d) the advection term goes to a very insignificant value, whereas the tendency term becomes very small. The balance, as is seen at 10 h, is between the Coriolis term and the vertical diffusion terms.

Summarizing, the dynamical balance of the individual terms along the depth can be described as follows.

In the x-momentum equation the balance in the upwelling region is mainly between the Coriolis term and the pressure gradient terms during the entire integration period. Mathematically,

$$\begin{aligned} fv = {} & -\frac{gHF}{L_x}\frac{\partial\zeta}{\partial\xi} + gH\alpha\left\{\int_\sigma^1 \frac{F\beta}{L_x}\frac{\partial \boldsymbol{T}}{\partial\xi}\,\mathrm{d}\eta - \frac{F}{L_x}\left[\frac{\partial\zeta}{\partial\xi}T_{\sigma=1} + \left(\frac{\partial h}{\partial\xi} - \sigma\frac{\partial H}{\partial\xi}\right)T\right]\right\} \\ & - gH\delta\left\{\int_\sigma^1 \frac{F\beta}{L_x}\frac{\partial \boldsymbol{S}}{\partial\xi}\,\mathrm{d}\eta - \frac{F}{L_x}\left[\frac{\partial\zeta}{\partial\xi}S_{\sigma=1} + \left(\frac{\partial h}{\partial\xi} - \sigma\frac{\partial H}{\partial\xi}\right)S\right]\right\}. \end{aligned} \tag{90}$$

Thus a quasi-geostrophic equilibrium exists. Accordingly, the development of the pressure gradient leads to the intensification of the baroclinic coastal jet from $t = 10$ to 96 h. In the seaward region ($x = 90$ km) the main balance is between the Coriolis force and the barotropic pressure gradient. Also, near the surface and bottom there is a significant contribution from the vertical diffusion term. Mathematically,

$$fv = -\frac{gHF}{L_x}\frac{\partial\zeta}{\partial\xi} + \frac{1}{H^2\beta}\frac{\partial}{\partial\eta}\left(\frac{K_{\mathrm{M}}}{\beta}\frac{\partial \boldsymbol{u}}{\partial\eta}\right). \tag{91}$$

As there is no horizontal temperature gradient, which results in the absence of the baroclinic pressure gradient term, the alongshore velocity is smaller and its rate of increase is also small compared with that of the upwelling region.

In the y-momentum equation it seem that no simple balance relation exists in the upwelling region. In the seaward region the advection term is negligible throughout the integration period. From $t = 10$ to 96 h the balance is between the Coriolis term and the vertical diffusion term. Thus

$$\frac{\partial v}{\partial t} + fu = \frac{1}{H^2\beta}\frac{\partial}{\partial\eta}\left(\frac{K_{\mathbf{M}}}{\beta}\frac{\partial \boldsymbol{v}}{\partial\eta}\right). \tag{92}$$

6.3. Experiment 2. Variable depth case

In this experiment a variable depth is incorporated into the model to examine the behaviour of the model with respect to a particular location in the field. The model is applied to the east coast of India at a plane perpendicular to the coast of Visakhapatnam. The depth contours off Visakhapatnam are used as the topography data for the model. Thus $h(x)$ is about 115 m at 55 km off Visakhapatnam and beyond but reduces to zero at the coast. No external alongshore pressure gradient is applied; thus the accelerations produced by the surface wind stress are higher than those of the observation.

6.3.1. Circulation and thermal structures. Figure 15 gives the circulation and thermal structure at $t = 10$ h. Figure 15a shows an offshore thermal advection and outcropping of the 27 °C contour at the surface at an offshore distance of 40 km. Upwarping of the isotherms can be seen up to 30 m. Near the coast the 26, 25, 24 and 23 °C isotherms are showing upwarping. Both a surface mixed layer and a bottom mixed layer are formed as a result of vertical turbulent mixing. The formation of the bottom mixed layer together with the topographic variation leads to the intersection of the 14 °C isotherm with the bottom topography. Figure 15b shows that an offshore flow takes place in the surface layer and an onshore flow takes place in the bottom layer, as in Experiment 1. The offshore

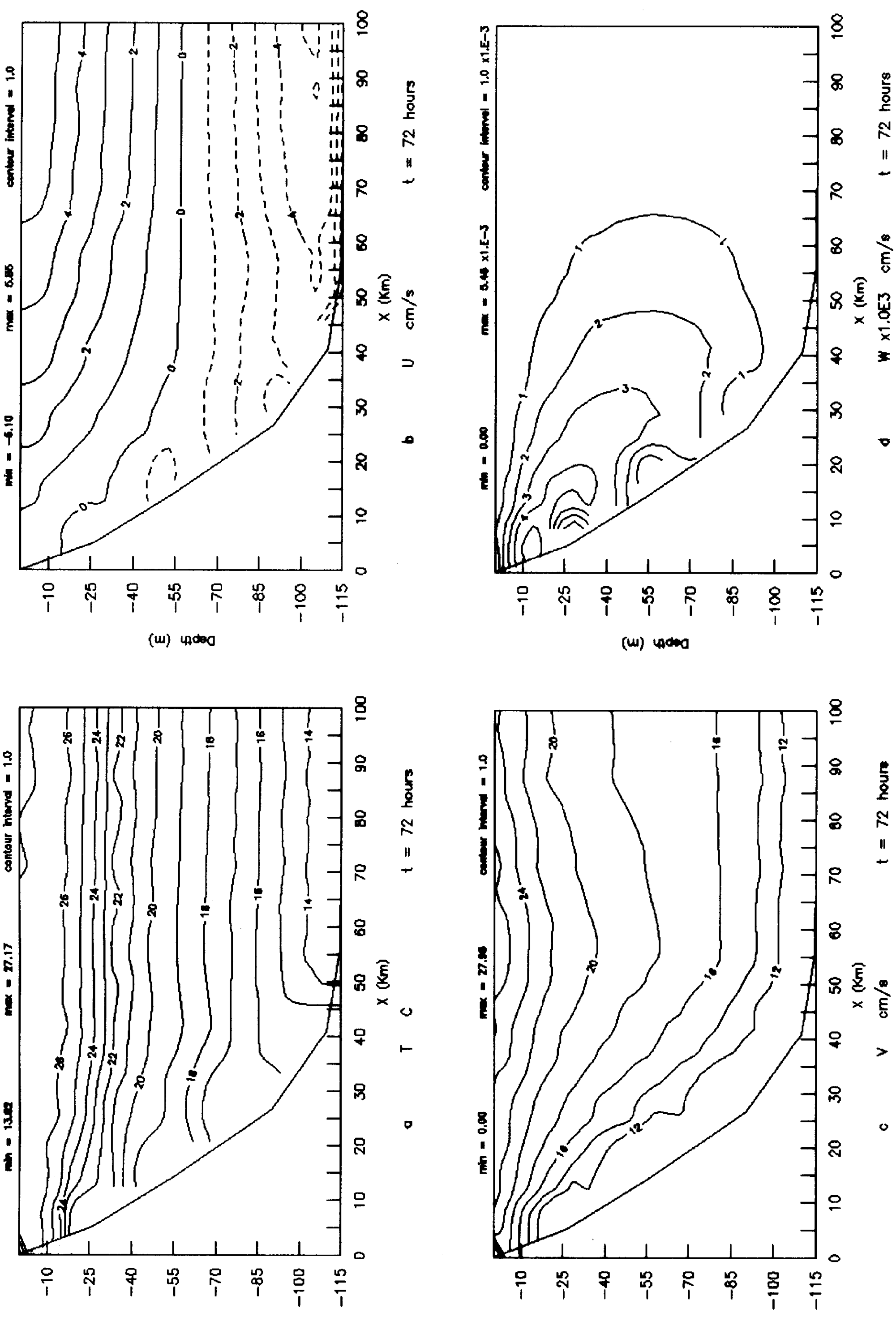

Figure 18. As Figure 15 but at 72 h

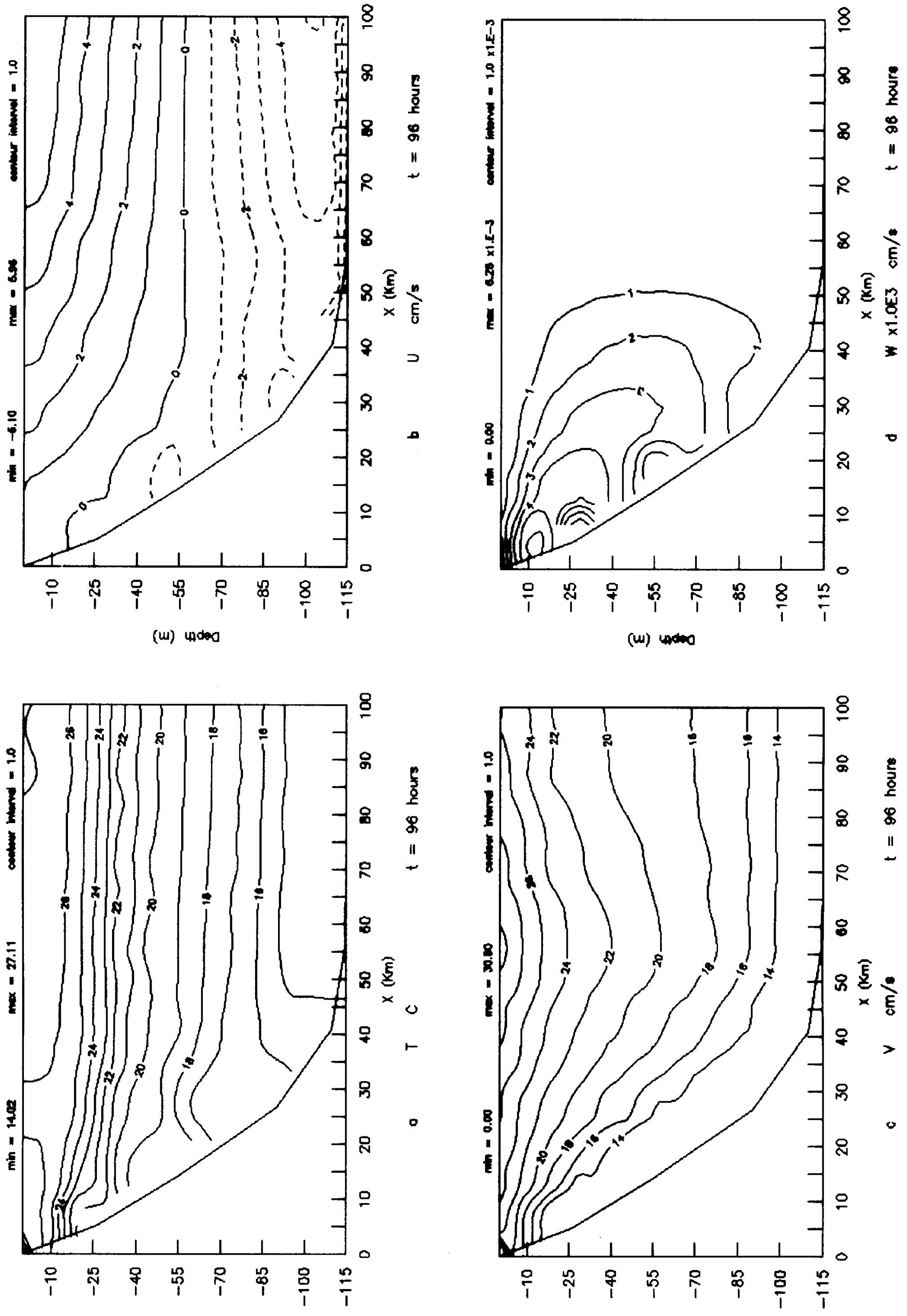

Figure 19. As Figure 15 but at 96 h

flow is found to be stronger near the coast owing to the shallowness of the water, having a maximum velocity of 3·0 cm s^{-1}. The formation of a weak bottom Ekman layer is observed with a very small vertical shear. The alongshore velocity given in Figure 15c shows that the baroclinic coastal jet has shifted farther offshore, with a maximum of 13 cm s^{-1} occurring at an offshore distance of 60 km. The jet, compared with that in Experiment 1, is broader and has a very small vertical shear associated with it.

Examination of Figure 16 indicates that the upwelling is strengthened at $t = 24$ h. Figure 16a, which gives the thermal structure, shows that the 27 °C isotherm outcrops at the surface farther offshore at 45 km. The upwarping of the isotherms has extended to a depth of 60 m. At the bottom the development of the Ekman layer has led to the formation of a bottom mixed layer with a depth of 10 m. The surface mixed layer is found to be of 15 m depth. Figure 16b shows the intensification of the onshore velocity in the bottom layers, with a maximum of 3·5 cm s^{-1}, increasing the shear in the bottom Ekman layer. The onshore velocity core near the coast has disappeared and it is thus found to be only an instantaneous feature due to a transient phase resulting from inertial application of the wind stress. A significant change in the onshore flow has occurred in the offshore region, where a bottom Ekman layer has developed during this period. This shows that the bottom topography induces two different time scales for the development of Ekman layers in nearshore and offshore regions. The alongshore velocity structure given in Figure 16c shows further intensification of the baroclinic coastal jet and correspondingly the vertical shear. It is found that the coastal jet has a maximum velocity of 17 cm s^{-1}. The position of the core has moved offshore consistent with the offshore thermal advection. The important feature in the vertical velocity structure of Figure 16d is the appearance of two upwelling centres. These upwelling centres are located around depths of 12 and 30 m respectively. The appearance of the two upwelling centres is in agreement with the results of Li.[10] The shallowness of the water near the coast results in a narrower width of the coastal upwelling, which is in accordance with the fact that the baroclinic radius of deformation is directly proportional to the depth. The vertical velocity is strengthened and has a maximum of $4{\cdot}5 \times 10^{-3}$ cm s^{-1} centred near the coast at a depth of 15 m. The other two upwelling centres are also strengthened in comparison with the 10 h result. The upwelling has spread to an offshore distance of 50 km, with the strong velocities being confined to the bottom topography and within 20 km from the coast and up to a depth of 60 m.

The circulation and thermal structure at $t = 48$ h are shown in Figure 17. The onshore–offshore structure given in Figure 17b reveals that the bottom Ekman layer is fully developed and the onshore velocity has reached a maximum of 4·9 cm s^{-1}. The offshore velocity has a maximum of 5·5 cm s^{-1} at a depth of 55 m on the seaward side. Near the coast, offshore velocities appear up to a depth of 12 m. Observation of Figure 17c reveals that the alongshore velocity has been further strengthened and has a maximum of 23·6 cm s^{-1} centred at an offshore distance of 15 km. The vertical shear in the alongshore velocity is high near the surface layers and decreases towards the mid-depths. The temperature structure given in Figure 17a reveals that a mixed layer of 15 m depth with the 27 °C isotherm has migrated further offshore to a distance of 60 km. The upwarping isotherms shows up to a depth of 70 m and the 17 °C isotherm also shows the upward tilt near the coast. The vertical velocity has decreased in strength during the integration period between $t = 24$ and 48 h, as observed from Figure 17d. The maximum occurs at the same depth as at $t = 24$ h but having a magnitude of $4{\cdot}7 \times 10^{-3}$ cm s^{-1}. The upwelling has spread to a distance of 60 km.

Figure 18 gives the flow and thermal structure at $t = 72$ h. The offshore thermal advection as seen in Figure 18a has pushed the 27 °C isotherm to 80 km offshore. The development of the bottom Ekman layer has resulted in intersection of the 14 and 15 °C isotherms with the bottom topography. The surface layer has now deepened and has a depth of 20 m. Intensification of the upwelling can be

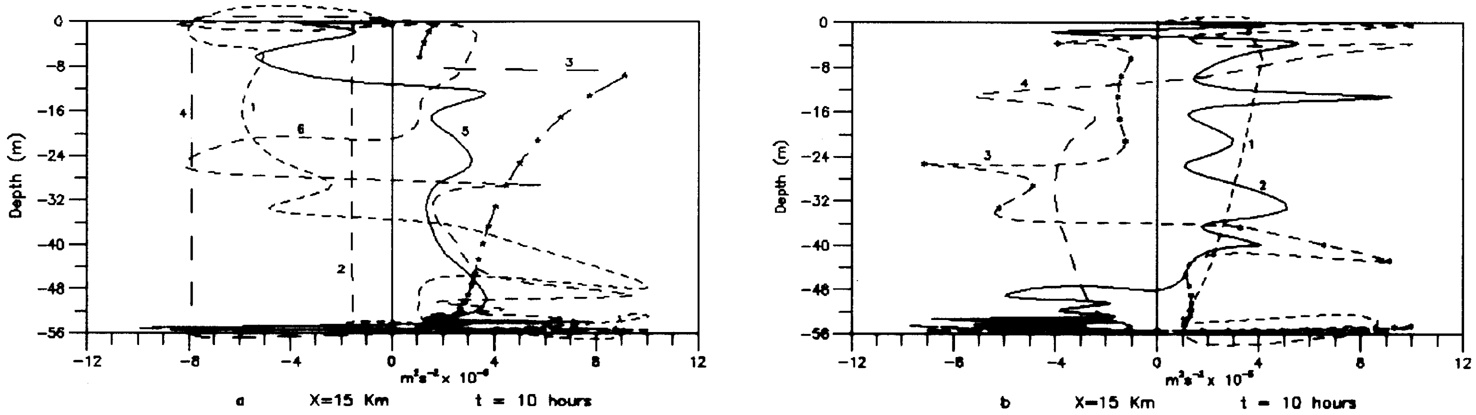

Figure 20. Vertical distribution at 10 h and 15 km offshore of terms in (a) *x*-momentum equation and (b) *y*-momentum equation

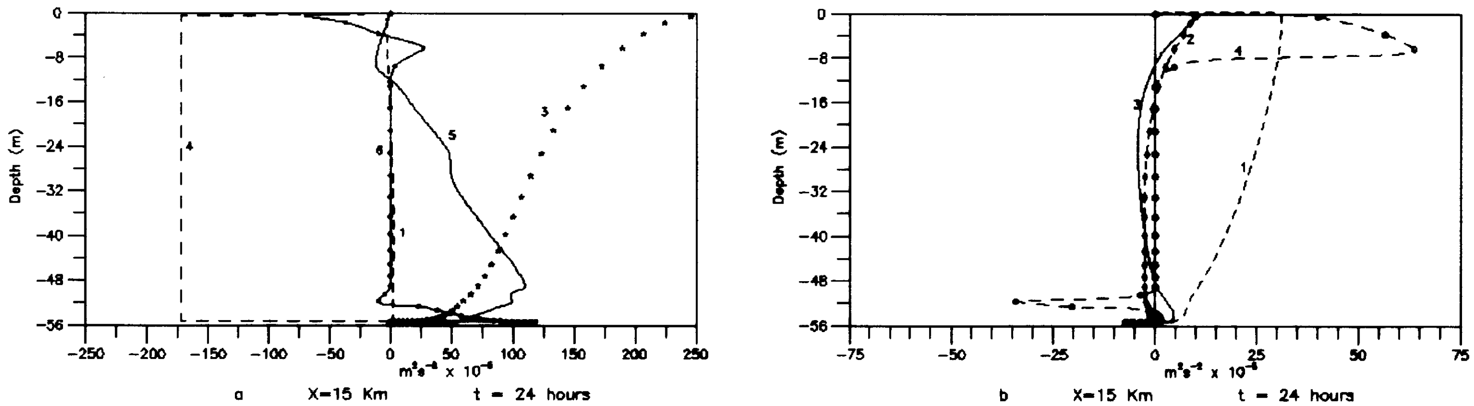

Figure 21. As Figure 20 but at 24 h

seen in terms of upwarping of the isotherms near the coast. The onshore–offshore flow structure given in Figure 18b reveals the strengthening of the onshore flow with a fully developed Ekman layer. The strength of the offshore flow is 5·4 cm s^{-1}, which is slightly higher than that at $t = 48$ h, whereas the onshore flow at the bottom has increased to $5{\cdot}1 \times 10^{-3}$ cm s^{-1}. The baroclinic coastal jet has a magnitude of 27 cm s^{-1} located 55 km offshore, compared with 23 cm s^{-1} at $t = 48$ hours. The vertical velocity is 5×10^{-3} cm s^{-1} in magnitude and only two centres of maxima appear as in Figure 18d. Even though the position of maximum vertical velocity appears at the same location, the upwelling has spread over an offshore distance of 70 km, the farthest being at the mid-levels (about 55 m depth), which coincides with the zero offshore velocity.

The circulation and thermal structure given in Figure 19 corresponds to $t = 96$ h. The temperature structure in Figure 19a shows that a small warm water region has formed near the coast, as the 26 °C isotherm intersects the free surface at 35 km offshore. The 27 °C isotherm is barely seen in the analysis area as it is moved out owing to both advection and diffusion processes. The onshore and offshore velocities (Figure 19b) are reduced in magnitude. The coastal jet in the alongshore velocity (Figure 19c) has a magnitude of 30 cm s^{-1} and the vertical shear extends to a depth of 55 m. The vertical velocity structure revealed in Figure 19d shows further weakening and the maximum of $6{\cdot}25 \times 10^{-3}$ cm s^{-1} occurs at a depth of 55 m and an offshore distance of 20 km. The intense part of the upwelling falls within an offshore distance of 30 km, which is nearly the baroclinic radius of deformation.

6.3.2. Balance analysis. A momentum balance analysis is performed on the x- and y-momentum equations along similar lines to that described in Section 6.2.2. As the far offshore point ($x = 90$ km) has a depth of 115 m, similar to that in Section 6.2.2, the momentum balance is observed to be the same. Thus the discussion here is restricted to the upwelling region, which is taken to be representative at $x = 15$ km. The terms are numbered as in Section 6.2.2.

Figure 20a gives the balance relation between the various terms in the x-momentum equation at $t = 10$ h. The advection term is negligible as it is two orders lower in magnitude compared with the other terms. It can be seen that the vertical diffusion term is very small except in the regions near the surface and bottom. Leaving apart the redions of frictional dissipation, the balance is mainly between the Coriolis term 3 and the pressure gradient terms 4 and 5. The difference between Figures 20a and the corresponding 10 h result in Section 6.2.2 is that the baroclinic part of the pressure gradient term, although pointing offshore, is reduced in the depth region of 30 m. The terms overall have a smaller magnitude compared with that of Section 6.2.2. In the y-momentum equation (Figure 20b) the vertical distribution of terms shows that the vertical diffusion term 4 has a large magnitude at the surface. The momentum term magnitude is significant compared with that in the y-momentum equation of Section 6.2.2. The Coriolis term points onshore near the surface but changes to offshore as the depth increases. The tendency term is large near the surface but gradually reduces to zero at the bottom. The lack of balance between the Coriolis and vertical diffusion terms results in a large magnitude of the tendency term, which indicates a strong baroclinic coastal jet. As the upwelling is in the development phase, the balance is well-established, as is evident from Figure 20.

Figure 21 gives the balance relation between the various terms at $t = 24$ h. In the x-momentum equation (Figure 21a) the balance is maintained as at $t = 10$ h. The magnitude of the terms is increased compared with that at $t = 10$ h. The baroclinic pressure gradient term points offshore and its magnitude increases with depth, reaching a maximum value of 110×10^{-5} m^2 s^{-2} at a depth of 45 m. The balance is well-established, leading to a weakening of the tendency term, which has a small value near the surface and becomes insignificant at the bottom. The vertical diffusion term is only a fraction of the other terms, contributing to the balance only at the surface and bottom. In the y-momentum equation (Figure 21b) the vertical distribution of the terms show that the Coriolis and

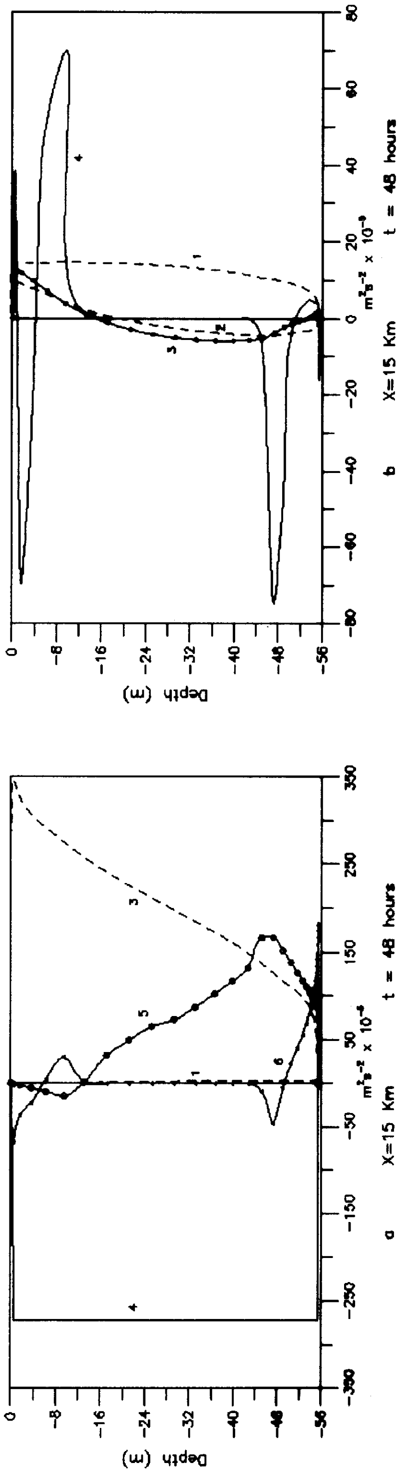

Figure 22. As Figure 20 but at 48 h

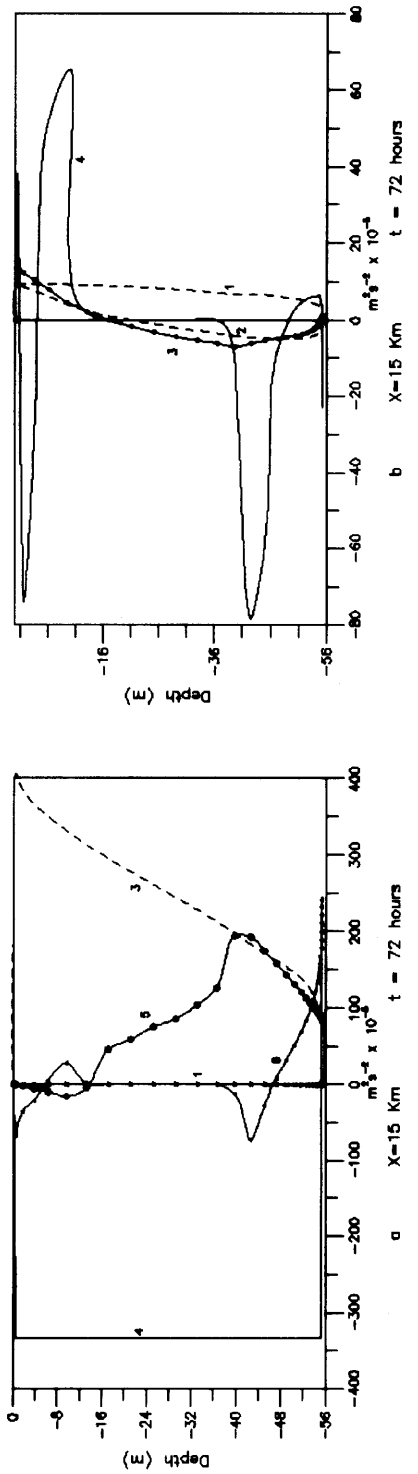

Figure 23. As Figure 20 but at 72 h

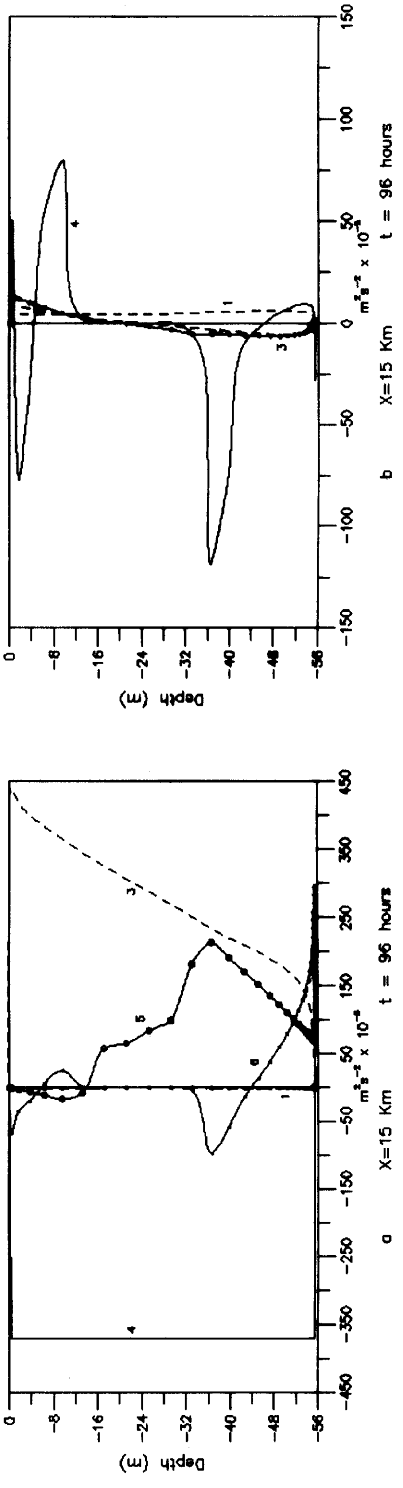

Figure 24. As Figure 20 but at 96 h

advection terms are much smaller compared with the result at $t = 10$ h. The tendency term, which results mainly from the imbalance of the vertical diffusion term 4 and the Coriolis term 3, is positive, with a maximum value near the surface. The magnitude of the vertical diffusion term is large at the surface, pointing offshore, but rapidly decreases to point onshore at 5 m depth. It turns again to point offshore before reducing to an insignificant value at 11 m depth.

Figures 22a–24a show the vertical distribution of the terms of the x-momentum equation at 48, 72 and 96 h respectively. The magnitude of the terms increases with increasing integration time. The vertical diffusion term rapidly increases in magnitude near the bottom, contributing to the momentum balance below 31 m depth at $t = 96$ h. It is observed that the maximum value of the baroclinic pressure gradient term also occurs at higher depths, successively from 24 to 31 m from the integration time $t = 48$ to 96 h respectively. As the balance is established, the tendency term is reduced in magnitude and becomes insignificant at $t = 96$ h.

REFERENCES

1. E. C. Lafond, ‘Oceanographic studies in the Bay of Bengal’, *Proc. Indian Acad. Sci. B*, **46**, 1–47 (1957).
2. T. V. N. Rao, B. P. Rao and V. S. R. Raju, ‘Upwelling and sinking along the Visakhapatnam coast’, *Indian J. Marine Sci.*, **15**, 84–87 (1986).
3. J. Pedlosky, ‘A non-linear model of the onset of upwelling’, *J. Phys. Oceanogr.*, **8**, 109–177 (1978).
4. J. S. Allen, ‘Upwelling and coastal jets in a continuously stratified ocean’, *J. Phys. Oceanogr.*, **3**, 245–257 (1973).
5. J. P. McCreary, ‘A linear stratified model of the equatorial undercurrent’, *Philos. Trans. R. Soc. London. A*, **298**, 603–635 (1981).
6. J. J. O’Brien and H. E. Hurlbert, ‘A numerical model of coastal upwelling’, *J. Phys. Oceanogr.*, **2**, 14–26 (1972).
7. B. Johns, S. K. Dube, P. C. Sinha, U. C. Mohanty and A. D. Rao, ‘Simulation of storm surges using a three-dimensional numerical model: an application to the 1977 Andhara cyclone’, *Q. J. R. Meteorol. Soc.*, **109**, 211–224 (1983).
8. N. A. Phillips, ‘A coordinate system having some special advantages for numerical forecasting’, *J. Meteorol.*, **14**, 184–185 (1957).
9. N. G. Freeman, A. M. Hale and M. B. Danard, ‘A modified sigma equations approach to the numerical modelling of Great Lake hydrodynamics’, *J. Geophys. Res.*, **77**, 1050–1060 (1972).
10. Z. Li, ‘A numerical study of basic coastal upwelling processes’, *Ph.D. Thesis*, University of Reading, 1990.
11. P. K. Kundu, ‘Numerical calculations of coastal flow with turbulence dynamics’, *Deep-Sea Res.*, **31**, 39–60 (1984).
12. P. K. Kundu, R. E. Thompson, B. M. Hickey and P. H. LeBlond, ‘Interaction of internal waves and mean flow observed near a coast’, *J. Marine Res.*, **46**, 1–23 (1988).
13. G. L. Mellor, ‘Analytical prediction of properties of stratified planetary surface layers’, *J. Atmos. Sci.*, **30**, 1061–1069 (1973).
14. H. Mosby, ‘Experiments on bottom friction’, *Bergens Mus. Aarb*, (10) (1949); P. Bowles, R. H. Burns, F. Hudswell and R. T. P. Whipple, ‘Sea disposal of low activity effluent’, *Proc. 2nd Int. Conf. on Peaceful Uses of Atomic Energy*, Vol. 18, United Nations, New York, 1958, p. 376.
15. H. Charnock, ‘Tidal friction from currents near the sea bed’, *Geophys. J.*, **2**, 215–221 (1959).
16. A. Arakawa and V. R. Lamb ‘Computational design of the basic dynamical processes of the UCLA general circulation model’, in J. Chang (ed.), *Methods in Computational Physics*, Vol. 17, Academic, New York, 1977, pp. 174–264.
17. S. Hastenrath and P. J. Lamb, *Climate Atlas of the Indian Ocean. Part 1. Surface Climate and Atmospheric Circulation*, University of Wisconsin Press, Madison, WI, 1979.